

A precise conformally mapped method for water waves in complex transient environments

Andreas H. Akselsen

*SINTEF Ocean, Department of Ship and Ocean Structures**

February 2025

Abstract

A two-dimensional water wave model based on conformal mapping is presented. The model is exact in the sense that it does not rely on truncated series expansions, nor suffer any numerical diffusion. Additionally, it is computationally highly efficient as it numerically evaluates only the surface line while using a fixed number of FFT operations per time step. A double layered mapping enforces prescribed outer boundaries without iteration. The model also supports transient boundaries, including walls. Mapping models are presented that support smooth bathymetries and angled overhanging geometries. An exact piston-type wavemaker model demonstrates the method's potential as a numerical wave tank. The model is tested and validated through a number of examples covering shallow water waves, wavemaker generation, rising bathymetry shelves, and wave reflection from slanting structures. A paddle-type wavemaker model, developed from the present theory, will be detailed in a forthcoming paper.

1 Introduction

Numerical modelling is taking an ever-larger role in theoretical and applied water wave studies. Although often seen as substitute for physical experiments, numerical models frequently feature in a complimentary capacity, providing validation and a supplementary information. In fact, *digital twins* of this kind are not limited to just mimicking experiments but can be incorporated into them; time-reversed simulation is a promising new wavemaker control strategy for reproducing extreme events in a controlled environment (Houtani et al., 2018; Ducroz et al., 2020).

In numerical wave tanks, both the free surface and transient boundaries are to be modelled. Commonly applied methods include the Boundary Element Methods (BEM) (Khait and Shemer, 2019), Finite Difference and Finite Element Methods (FDM/FEM) using dynamic sigma-gridding (Wu and Taylor, 1995; Wang et al., 2022), and Higher Order Spectral methods (HOS) (Bonnetoy et al., 2006). The latter provides superior efficiency at approximate accuracy.

Complex boundary shapes manifest in both coastal environments and basins alike, be it in the form of naturally varying bathymetries or structural components and machinery. BEM's and sigma-gridded methods support most domain shapes but at lower computationally efficient than HOS methods. HOS methods can in turn be made to

*Paul Fjermstads vei 59, 7052 Trondheim, Norway.

approximately represent bathymetry variations at some expense to efficiency (Gouin et al., 2016, 2017).

Historically, conformal mapping has played a crucial role in the study of hydrodynamics (Lamb, 1932; Milne-Thomson, 1962), numerical computing power being limited. In the context of free-surface flows, it has often been used to characterise surface undulations caused by flow (e.g., Forbes and Schwartz, 1982; Dias and Vandenberg, 1989). More recently, a highly efficient and precise algorithm for describing solitary waves has been developed using conformal mapping (Clamond and Dutykh, 2013; Dutykh and Clamond, 2014; Clamond et al., 2015) and later extended to model Stokes waves at arbitrary water depths (Dutykh et al., 2016; Clamond and Dutykh, 2018). This open-source algorithm surpasses traditional perturbation theory solutions for Stokes and cnoidal waves in both accuracy and range of validity and has been extensively used in this work to set up initial simulation conditions.

The model presented here builds on the flat-bedded conformal mapping approach of Chalikov and Sheinin (1996), further developed in Chalikov and Sheinin (2005); Chalikov (2016, 2020) and Zakharov et al. (2002). Depth variation was incorporated in a similar model by Viotti et al. (2014) that uses a fixed-point iteration scheme to simultaneously resolve the unknown surface and the prescribed bathymetry in a single mapping. However, this iterative approach significantly reduced efficiency. A key novelty of the present model is the use of a double-layered mapping as illustrated in Figure 1. By separating prescribed boundary coordinates from the dynamic free-surface coordinates, this approach eliminates the need for iteration while maintaining exactness. The resulting method is found to resemble the one by Ruban (2004, 2005) who effectively also adopts a double mapping.

Domain shape and motions are prescribed by design of the first mapping layer. We outline two families of prescribed mappings, one based on Fourier decomposition, suitable for smooth single-valued bathymetries, and another based on the Schwarz–Christoffel theorem, which accommodates sharp angles. The latter particularly useful for modelling structural features and supports overhanging geometries, provided they remain topologically connected to the outer boundary. Mappings may be transient, allowing for the representation of moving machinery or evolving geophysical features.

Conformal mapping enables concise evaluation of time-dependent boundaries, seemingly ideal for representing a moving environment with versatility, accuracy *and* efficiency. Like the HOS method, it makes use of the Fast Fourier Transformation algorithm (FFT) while representing the interior domain analytically, requiring computation only along the free surface line. Unlike HOS, however, it retains exact formal accuracy without relying on truncated series expansions or suffering from numerical diffusion. Higher levels of nonlinearity do not necessitate additional model terms, making conformal mapping particularly advantageous in shallow waters where nonlinear effects are strong.

A fundamental limitation of conformal mapping, unlike HOS methods, is its restriction to two-dimensional wave fields. While ideal for wave flumes and long-crested waves, two-dimensional modelling cannot fully capture the long-term evolution of directional wave fields (Chalikov and Babanin, 2013; Chalikov, 2016). The difference affects long-term energy transfer across length scales (analogue to turbulence) and extreme wave statistics (Hennig et al., 2015). The wave breaking behaviour is also

different in short-crested waves (McAllister et al., 2024) and the structural loads they produce. While three-dimensional conformal mapping is theoretically possible, it is so far more mathematically complex and rarely pursued. Instead, boundary integral methods, which approximate three-dimensional conformal transformations, are more commonly employed.

This paper aims to demonstrate that, despite its abstraction, the conformal mapping strategy is highly applicable to practical studies of wave dynamics and numerical wave tank simulations. To illustrate its versatility, a range of examples are presented, including shallow-water waves, breaking waves, interactions with complex geometries, transient bathymetries, and wave generation by wavemakers. These are all detailed in section 4, following the wave model in section 2 and domain mapping models in section 3. Closing remarks are provided in section 5.

2 The double-layered Conformally Mapped Model

2.1 Mapping description

The conformal mapping approach simplifies evaluation of complex boundaries such as sketched in Figure 1a. Consider a moving domain boundary, $\partial\mathcal{Z}(t)$, along which we aim to enforce a kinematic condition of impermeability. A general means of doing so is through a fluid particle position $z^p(t)$ advected with the fluid velocity. The condition states that a particle initially located at the boundary will remain there:

$$z^p(t) \in \partial\mathcal{Z}(t) \text{ provided } z^p(0) \in \partial\mathcal{Z}(0). \quad (1)$$

While valid, this formulation is cumbersome to work with directly, motivating the use of conformal mapping Maps are sought which can project an arbitrarily complex transient domain into a fixed rectangle or strip $\bar{\bar{\mathcal{Z}}}$ (Figure 1c) where (1) can be explicitly evaluated.

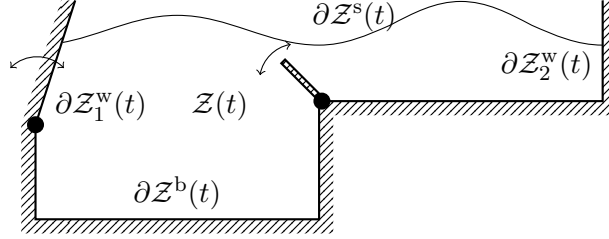
Harmonic maps have the characteristic of mutually dependent coordinates in the sense that shifting one will affect all others. While the bed and wall boundaries are assumed prescribed, the free surface evolves dynamically and cannot be predetermined. Mapping all boundaries simultaneously would therefore require continuous adjustments, for example using iteration as in Viotti et al. (2014). To circumvent the need for iteration, we introduce an intermediate mapping layer \bar{z} (Figure 1b) in which all prescribed boundaries are fixed straight lines. The free surface is then mapped to a straight surface line in a third rectangular $\bar{\bar{z}}$ -plane (Figure 1c). Impermeability now ensures that any movement on the boundary $\partial\bar{\bar{\mathcal{Z}}}$ remains purely tangential such that boundary points remain on the prescribed contour in accordance with the kinematic condition (1).

The mapping $\bar{\bar{z}} \mapsto \bar{z} \mapsto z$ is represented through functions \bar{f} and $\bar{\bar{f}}$,

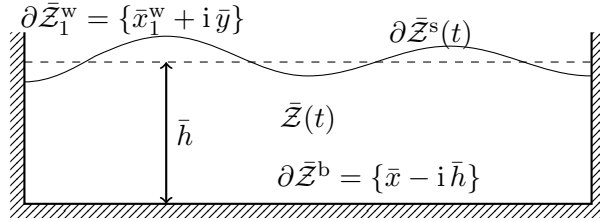
$$z = \bar{f}(\bar{z}, t), \quad \bar{z} = \bar{\bar{f}}(\bar{\bar{z}}, t), \quad (2)$$

and we introduce the conversion throughout of marking functions that take \bar{z} and $\bar{\bar{z}}$ -coordinate arguments with the same single and double bar notation, respectively. This conformal mapping approach works efficiently because simulation is performed entirely from the $\bar{\bar{z}}$ -plane, never requiring inverse mapping apart from setting up initial

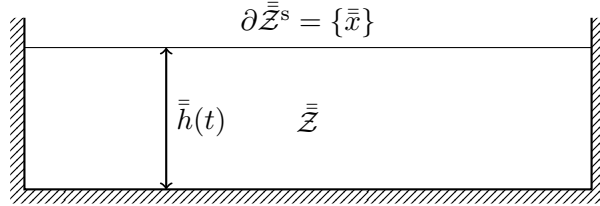
conditions. The simulation routine, as well as the mapping of the final solution, is then entirely explicit.



(a) Physical z -plane.



(b) Prescribed \bar{z} -plane.



(c) Rectangular $\bar{\bar{z}}$ -plane.

Figure 1: Sketch of the Z , \bar{Z} and $\bar{\bar{Z}}$ -domains.

The prescribed mapping function $\bar{f}(\bar{z}, t)$, describing walls, bathymetry and imposed external motions, is expressed numerically or analytically prior to simulation. Two families of mapping functions, detailed in [subsection 3.1](#), accommodate a broad range of application. In cases where periodic boundaries replace solid walls, the \bar{z} -plane transforms into a periodic strip. A third possibility, as noted by [Ruban \(2005\)](#), is a shore edge type of boundary. This is achieved by letting $\bar{f}(\bar{z}, t)$ asymptotically tend towards a single point $C_{\pm}(t)$: $\bar{f}(\bar{z}, t) \rightarrow C_{\pm}(t)$ as $\bar{x} \rightarrow \pm\infty$. Shore boundaries have not been tested in the present study.

Fluid velocities are represented using the complex potential $w = \phi + i\psi$, ϕ being the fluid velocity potential and ψ its harmonic conjugate, the stream function. By virtue of conformality, these functions transfer directly between planes,

$$\bar{w}(\bar{z}, t) = w[\bar{f}(\bar{z}, t), t], \quad \bar{\bar{w}}(\bar{\bar{z}}, t) = \bar{w}[\bar{\bar{f}}(\bar{\bar{z}}, t), t], \quad (3)$$

while still satisfying the Laplace equation. Differentiation now yields the following key properties:

$$\begin{aligned} w_z &= \bar{w}_{\bar{z}} / \bar{f}_{\bar{z}}, & w_t &= \bar{w}_t - \bar{w}_{\bar{z}} \bar{f}_t / \bar{f}_{\bar{z}}, \\ \bar{w}_{\bar{z}} &= \bar{\bar{w}}_{\bar{\bar{z}}} / \bar{\bar{f}}_{\bar{\bar{z}}}, & \bar{w}_t &= \bar{\bar{w}}_t - \bar{\bar{w}}_{\bar{\bar{z}}} \bar{\bar{f}}_t / \bar{\bar{f}}_{\bar{\bar{z}}}. \end{aligned} \quad (4)$$

In anticipation of wall conditions to come, we also introduce an arbitrary pre-determined background potential $W(z, t)$, the total potential then being $w + W$. The background potential is relevant only for transient wall boundaries and vanishes ($W = 0$) when walls are stationary or periodic. A similar background field was introduced by [Ducrozet et al. \(2016\)](#); however, our approach differs in that it maintains exactness. The background potential is imposed in the \bar{z} -plane, where wall boundaries are steady and the mapping predetermined; $\bar{W}(\bar{z}, t) = W[\bar{f}(\bar{z}, t), t]$. Defined the same way, \bar{W} also obeys the differentiation rules stated above.

2.2 The kinematic boundary condition

The kinematic boundary condition (1) can now be reformulated in the rectangular \bar{z} plane where evaluation is more convenient. The position of a fluid particle $z^P(t)$ of (1) maps directly between the different coordinate systems:

$$z^P(t) = \bar{f}[\bar{z}^P(t), t], \quad \bar{z}^P(t) = \bar{f}[\bar{z}^P(t), t]. \quad (5)$$

This leads us to the notion of a particle velocity \mathcal{U} as viewed in the z -plane, as well as *apparent particle velocities* $\bar{\mathcal{U}}$ and $\bar{\bar{\mathcal{U}}}$ as viewed in the intermediate \bar{z} and final $\bar{\bar{z}}$ -plane, respectively. Using (4) and (5), we obtain

$$\mathcal{U} \equiv \frac{dz^P}{dt} = w_z^* + W_z^*, \quad (6a)$$

$$\bar{\mathcal{U}} \equiv \frac{d\bar{z}^P}{dt} = \frac{\mathcal{U} - \bar{f}_t}{\bar{f}_z} = \frac{\bar{w}_z^* + \bar{W}_z^*}{|\bar{f}_z|^2} - \frac{\bar{f}_t}{\bar{f}_z}, \quad (6b)$$

$$\bar{\bar{\mathcal{U}}} \equiv \frac{d\bar{\bar{z}}^P}{dt} = \frac{\bar{\mathcal{U}} - \bar{\bar{f}}_t}{\bar{\bar{f}}_z} = \frac{\bar{\bar{w}}_z^*}{|\bar{\bar{f}}_z|^2 |\bar{f}_z|^2} + \frac{1}{\bar{\bar{f}}_z} \left(\frac{\bar{W}_z^*}{|\bar{f}_z|^2} - \frac{\bar{f}_t}{\bar{f}_z} - \bar{\bar{f}}_t \right), \quad (6c)$$

asterisk denoting complex conjugation. In the $\bar{\bar{z}}$ -plane, kinematic boundary condition (1) simplifies to

$$\text{Im } \bar{\bar{\mathcal{U}}}(\bar{\bar{x}}, t) = 0, \quad \text{Im } \bar{\bar{\mathcal{U}}}(\bar{\bar{x}} - i\bar{\bar{h}}, t) = -\bar{\bar{h}}_t, \quad (7a)$$

and, if walls are present along $x = \bar{x}_1^W$ and \bar{x}_2^W ,

$$\text{Re } \bar{\bar{\mathcal{U}}}(\bar{x}_1^W + i\bar{y}, t) = 0, \quad \text{Re } \bar{\bar{\mathcal{U}}}(\bar{x}_2^W + i\bar{y}, t) = 0. \quad (7b)$$

We further have that $\bar{\bar{f}}_t$ is real at the bed and pure imaginary at walls, and that $\bar{\bar{f}}_z$ is real along both bed and walls.

2.3 Wall boundaries

The present method employs discrete Fourier transformation, which inherently enforces periodic boundary conditions. If walls are prescribed, this property is further utilized to impose impermeability using the method of mirroring; consider a periodic variable $\bar{\mu}$ described along discrete positions $\{\bar{x}_i\}$ in a vector $[\bar{\mu}_1, \bar{\mu}_2, \dots, \bar{\mu}_n]$. Combined with Fourier decomposition, the property $\bar{\mu}_{\bar{x}} = 0$ is enforced along $\bar{x} = \bar{x}_1^W = \bar{x}_1$ and $\bar{x}_2^W = \bar{x}_N$ by extending the vector with its mirror image:

$$[\bar{\mu}_i] := [\bar{\mu}_1, \dots, \bar{\mu}_n, \bar{\mu}_{n-1}, \dots, \bar{\mu}_2]. \quad (8)$$

Here, $\bar{f}_{\bar{z}}(\bar{z}, t)$ is assumed to be real at the lateral boundaries implying no coordinate rotation. Similar to a padding routine, we mirror the inputs to Fourier transformation and remove the mirrored half following inverse transformation, as illustrated in [Listing 3](#) in the appendix. Alternatively, the folded domain can be simulated in its entirety, including the mirror plane upon initiation.

Mirroring effectively satisfies the impermeability condition (7b) as long as the wall boundaries remain stationary. If walls are moving, then (7b) along with (6b) defines a condition for the background potential \bar{W} , introduced for this purpose. The resulting condition is

$$\operatorname{Re} \bar{W}_{\bar{z}} = \operatorname{Re}(\bar{f}_{\bar{z}} \bar{f}_t^*) \quad \text{along } \bar{x} = \bar{x}_1^w \text{ and } \bar{x}_2^w. \quad (9)$$

2.4 Simulation

Next, we consider the kinematic condition (7a) along the free surface and the bed, both of which remain horizontal in the \bar{z} -plane. The requirement that the bed remains flat and steady¹ in the \bar{z} -plane implies that $\operatorname{Im} \bar{U} = 0$. Consequently, using (7a) and the second expression in (6c), we find that

$$\operatorname{Im} \left(\frac{\bar{f}_t}{\bar{f}_{\bar{z}}} \right)_{\bar{y}=-i\bar{h}} = \bar{h}_t(t). \quad (10)$$

This constitutes a condition on the bottom velocity field, which in the \bar{z} -plane, according to (7a) and (6c), becomes

$$\bar{\phi}_{\bar{y}}(\bar{x}, -\bar{h}, t) = \bar{f}_{\bar{z}} \operatorname{Im}(\bar{W}_{\bar{z}} - \bar{f}_{\bar{z}} \bar{f}_t^*) \Big|_{\bar{y}=-\bar{h}} \equiv \bar{\mu}^b(\bar{x}, t). \quad (11a)$$

In cases where the bed remains stationary, we simply have $\bar{\mu}^b = 0$. Conversely, at the free surface, the velocity potential is prescribed rather than the position, and we express (7a) and (6c) accordingly:

$$\operatorname{Im} \left(\frac{\bar{f}_t}{\bar{f}_{\bar{z}}} \right)_{\bar{y}=0} = -|\bar{f}_{\bar{z}} \bar{f}_{\bar{z}}|^{-2} \operatorname{Im} \left[\bar{w}_{\bar{z}} + \bar{f}_{\bar{z}} (\bar{W}_{\bar{z}} - \bar{f}_{\bar{z}} \bar{f}_t^*) \right] \Big|_{\bar{y}=0} \equiv \bar{\mu}^s(\bar{x}, t). \quad (11b)$$

Our method repeatedly relies on the projection kernels described in [Appendix A](#). Using these, the complex potential \bar{w} is projected onto the surface potential $\bar{\phi}^s = \bar{\phi}(\bar{x}, 0, t) = \operatorname{Re} \bar{w}(\bar{x}, t)$ and the bottom velocity condition (11a). In form of the velocity field, the projection is

$$\begin{aligned} \bar{w}_{\bar{z}}(\bar{z}, t) &= \frac{\partial}{\partial \bar{z}} \left[\mathcal{C}_{\bar{h}} * \bar{\phi}^s \right] (\bar{z}) - i \left[\mathcal{C}_{-\bar{h}} * \bar{\mu}^b \right] (\bar{z} + i\bar{h}) \\ &= \mathcal{F}^{-1} \left[\left(k \mathcal{F}(\bar{\phi}^s) e^{-k\bar{h}} - \mathcal{F}(\bar{\mu}^b) \right) i \operatorname{sech}(k\bar{h}) e^{-k\bar{y}} \right]. \end{aligned} \quad (12)$$

The latter expression illustrates the projection kernel, \mathcal{F} implying discrete Fourier transformation with wavenumbers k ; see [Appendix A](#) for details. A real constant may be added to this expression to superpose an irrotational current to the solution.

¹The requirement $\bar{h}_t = 0$, which simplifies expressions that follow, can always be accommodated by designs of $\bar{f}(\bar{z}, t)$.

Equation (11b) describes the evolution of the mapping function \bar{f} imposed by surface dynamics. Since bed coordinates must remain at $\bar{y} = -\bar{h}$ it follows that $\text{Im } \bar{f}_t(\bar{x} - i\bar{h}, t)$ is constant. According to Appendix A, the appropriated mapping is then

$$\frac{\bar{f}_t}{\bar{f}_{\bar{z}}} = i [\mathcal{S}_{\bar{h}}^* \bar{\mu}^s](\bar{z}) + u_0(t), \quad (13)$$

the real function $u_0(t)$ being arbitrary. The surface values $\bar{f}_t(\bar{x})$ are integrated in time to obtain $\bar{f}(\bar{x}, t)$, determining the evolution of the free surface at the next time step. To avoid numerical issues, it is advisable to march only the vertical surface component

$$\bar{\eta}(\bar{x}, t) = \text{Im} \left\{ \bar{f}(\bar{x}, t) \right\} \quad (14)$$

forwards in time and reconstruct $\bar{f}(\bar{x}, t)$ at the next time level. Since $\text{Im } \bar{f}(\bar{x} - i\bar{h}, t)$ is constant, the projection

$$\bar{f}(\bar{z}, t) = \bar{z} + i [\mathcal{S}_{\bar{h}}^* \bar{\eta}](\bar{z}) + \xi_0(t), \quad (15)$$

is appropriate, $\xi_0(t)$ being another arbitrary real function. Applying the kernel property (44d), we now determine the depth of the \bar{z} -plane as

$$\bar{h} = \bar{h} + \langle \bar{\eta} \rangle. \quad (16)$$

The remaining details of the kinematic condition now concerns the real functions $\xi_0(t)$ and $u_0(t)$ in (15) and (13), which must be chosen consistently. To do so, we consider the horizontal average² of \bar{f} and \bar{f}_t . Combining (13) and (15) and employing the projection kernel definitions, we find

$$\langle \bar{f} \rangle = i \langle \bar{\eta} \rangle + \langle \bar{z} \rangle + \xi_0(t), \quad (17a)$$

$$\langle \bar{f}_t \rangle = i \langle \mu \rangle + u_0(t) - \sum_{j=1}^M \frac{2k_j}{\sinh^2 k_j \bar{h}} \text{Im} [\mathcal{F}_j(\bar{\eta}) \mathcal{F}_{-j}(\bar{\mu}^s)]. \quad (17b)$$

To maintain a non-drifting frame we set $\xi_0(t) = 0$. Consistency is then maintained by having the two last terms of (17b) cancel. The easiest way to achieve this in practice is setting

$$u_0(t) = \text{Im} \left\langle \bar{f}_{\bar{z}} [\mathcal{S}_{\bar{h}}^* \bar{\mu}^s] \right\rangle. \quad (18)$$

In closed domains, the expression can be disregarded entirely, as the mirror symmetry of (8) ensures zero mean. Equations (10), (11b), (13), (14), (16), (17b), (44b) and (44d) are now consistent and yield the following relationships of conservation:

$$\text{Im} \left\langle \bar{f}_t \right\rangle = \langle \bar{\mu}^s \rangle = \text{Im} \left(\frac{\bar{f}_t}{\bar{f}_{\bar{z}}} \right)_{\bar{y}=-\bar{h}} = \langle \bar{\eta} \rangle_t = \bar{h}_t. \quad (19)$$

²defined $\langle \bar{\mu} \rangle = \int_0^{\bar{L}} \bar{\mu}(\bar{x} + i\bar{y}) d\bar{x} / \bar{L} = \mathcal{F}_0(\bar{\mu})$.

Having now established surface coordinates and velocities, the final step is to impose the dynamic boundary condition. In the z -plane, this is given the Bernoulli equation

$$\phi_t + \operatorname{Re} W_t + \frac{1}{2}|w_z + W_z|^2 + gy + p/\rho = 0 \quad (20)$$

evaluated along $\partial\mathcal{Z}^s$ where $p = 0$. Using (4), it is straightforward to rewrite (20) in terms of \bar{z} -variables:

$$\bar{\phi}_t = \operatorname{Re} \left[\frac{\bar{w}_{\bar{z}}}{\bar{f}_{\bar{z}}} \left(\bar{f}_t + \frac{\bar{f}_t}{\bar{f}_{\bar{z}}} \right) - \bar{W}_t + \bar{W}_{\bar{z}} \frac{\bar{f}_t}{\bar{f}_{\bar{z}}} \right] - \frac{1}{2} \left| \frac{\bar{w}_{\bar{z}}}{\bar{f}_{\bar{z}} \bar{f}_{\bar{z}}} + \frac{\bar{W}_{\bar{z}}}{\bar{f}_{\bar{z}}} \right|^2 - gy \quad (21)$$

evaluated along $\bar{y} = 0$ with coordinates mapped accordingly. The numerical examples presented are solved using a dynamic time-stepping ODE solver, which integrates either the physical or Fourier components of $\bar{\phi}_t^s$ and $\bar{\eta}_t$.³ Surface tension can be added to (21) without difficulty. This completes the simulated part of the conformal mapping model.

Listing 1 provides an excerpt of MATLAB code illustrating how the model may be implemented in practice. With stationary beds, each time step requires seven Fourier transformations, with an additional four needed for the stabilisation procedure described later. When modelling transient beds, three more transformations are required. In the special case of a flat bed, where $\bar{f}(\bar{z}, t) = \bar{z}$, the model simplifies to a compact version of the model by Chalikov and Sheinin (2005). When extended to transient bathymetries and infinite boundaries, the model aligns conceptually with that of Ruban (2005).

```

FFTeta = fft(eta);
hhh = hh + mean(eta); % eq 16
C = 2./(1+exp(2*k*hhh)); % eq A.1a
S = 2./(1-exp(2*k*hhh)); S(1) = 1; % eq A.1b
zz = xxx + 1i*ifft(S.*FFTeta); % eq 15
fff_zzz = 1 - ifft(S.*k.*FFTeta); % eq 15
J = abs(ff_zz(zz)).*fff_zzz.^(-2); % double inverse Jacobian
www_zzz = ifft(C.*1i.*k.*fft(pphi)); % eq 12
mu_s = -J.*imag(www_zzz); % eq 11b
ftfz = 1i*ifft(S.*fft(mu_s)); % eq 13 (ftfz = fff_t/fff_zzz)
ftfz = ftfz - mean(real(ftfz).*fff_zzz); % eq 18 (removes real mean from fff_t)
eta_t = imag(ftfz).*fff_zzz; % eq 14
pphi_t = real(www_zzz).*ftfz - .5*J.*abs(www_zzz).^2 - g*imag(ff(zz)); % eq 21

```

Listing 1: Implementation example (MATLAB syntax) assuming stationary prescribed map $\bar{f}(\bar{z})$ and periodic boundary conditions. Repeated characters replace the single and double bar notation. Anti-aliasing neglected.

2.5 Pressure

Pressure can be computed diagnostically during post-processing using the original Bernoulli equation (20) which provides both the unmapped potential time derivative ϕ_t at the surface, and the pressure within the fluid. As before, the conjugate of the potential time derivative corresponds to the time derivative of the stream function,

³Marching the Fourier variables in time requires fewer Fourier transformations but the ODE solver often responds better to physical variables.

which remains constant at the impermeable bed. The appropriate projection kernel is in this case $\mathcal{C}_{\bar{h}}$ leading to

$$\bar{p}(\bar{z}, t)/\rho = - \left[\mathcal{C}_{\bar{h}} * \bar{\phi}_t^s \right] (\bar{z}) - \frac{1}{2} \left| \frac{\bar{w}_{\bar{z}}}{\bar{f}_{\bar{z}} \bar{f}_{\bar{z}}} + \frac{\bar{W}_{\bar{z}}}{\bar{f}_{\bar{z}}} \right|^2 - gy. \quad (22)$$

Here, $\bar{\phi}_t^s$ equals the last two terms of (21) (or equivalently (22)) evaluated at the surface $\bar{y} = 0$. The flow potential and stream function are obtained directly from (12) through straightforward analytical integration, taking care to make the zero-mode proportional to \bar{z} .

An example of a reconstructed velocity and pressure field, derived from surface variables using equations (12), (15) and (22) is presented in Figure 6. Additional examples of velocity potentials are shown in Figure 16.

2.6 A model hybrid

A simpler alternative to the method presented thus far is a conformal mapping extension of the conversional (HOS) scheme, which served as a prototype for the present work. Although less precise, this approach is also less abstract and therefore worth outlining. In the prototype, simulations are conducted directly from the \bar{z} -plane, assuming a prescribed mapping function $\bar{f}(\bar{z})$. The mapping provides the rectangular domain for which the conventional HOS scheme is designed. Defining the surface potential $\bar{\phi}^s(\bar{x}, t) = \bar{\phi}[\bar{x}, \bar{y}^s(\bar{x}, t), t]$, where $\bar{y}^s(\bar{x}, t)$ describes the surface such that $\bar{x} + i\bar{y}^s(\bar{x}, t) \in \partial\bar{\mathcal{Z}}^s$, we obtain the governing equations

$$\bar{y}_t^s = |\bar{f}_{\bar{z}}|^{-2} \left[\bar{\phi}_{\bar{x}}^s \bar{y}_x^s - \left(1 + (\bar{y}_x^s)^2 \right) \bar{\phi}_{\bar{y}} \right] \quad \text{along } \bar{y} = \bar{y}^s(\bar{x}, t), \quad (23a)$$

$$\bar{\phi}_t^s = -\frac{1}{2} |\bar{f}_{\bar{z}}|^{-2} \left[(\bar{\phi}_{\bar{x}}^s)^2 - \left(1 + (\bar{y}_x^s)^2 \right) \bar{\phi}_{\bar{y}}^2 \right] - g \operatorname{Im} \bar{f} \quad \text{along } \bar{y} = \bar{y}^s(\bar{x}, t), \quad (23b)$$

$$\bar{\phi}_{\bar{y}} = 0 \quad \text{along } \bar{y} = -\bar{h}, \quad (23c)$$

$$\bar{\phi}_{\bar{x}} = 0 \quad \text{along } \bar{x} = \bar{x}_j^w \text{ (optional)}. \quad (23d)$$

Vertical surface velocity $\bar{\phi}_{\bar{y}}[\bar{x}, \bar{y}^s(\bar{x}, t), t]$ is computed using the conventional HOS scheme, employing Taylor and Stokes expansions. Moving boundaries can also be represented by a background potential, here omitted.

2.7 Stabilisation, anti-aliasing and beach damping

As with other spectral methods, stabilisation measures are necessary to suppress the buildup of high-frequency noise. Following Chalikov and Sheinin (2005), we adopt the modal damping approach

$$\bar{\eta}_t := \mathcal{F}^{-1} [\mathcal{F}(\bar{\eta}_t) - \hat{\nu} \mathcal{F}(\bar{\eta})], \quad \bar{\phi}_t^s := \mathcal{F}^{-1} \left[\mathcal{F}(\bar{\phi}_t^s) - \hat{\nu} \mathcal{F}(\bar{\phi}^s) \right]. \quad (24)$$

As in Chalikov and Sheinin (2005), the modal damping coefficient is modelled

$$\hat{\nu}(k) = r \sqrt{\frac{2\pi g}{\bar{L}}} \left(\frac{\max(|k| - k_d, 0)}{k_{\max} - k_d} \right)^2, \quad (25)$$

where k_d is an intermediate wavenumber, $k_{\max} \approx \pi n / \bar{L}$ is the largest wave number and \bar{L} is the horizontal length of the $\bar{\mathcal{Z}}$ -domain. This formulation enforces no damping

up to the intermediate wavenumber, after which damping increases quadratically up to a fixed value. Typical choices are $k_d = 0.5 k_{\max}$ and $r = 0.1$ or 0.25 .

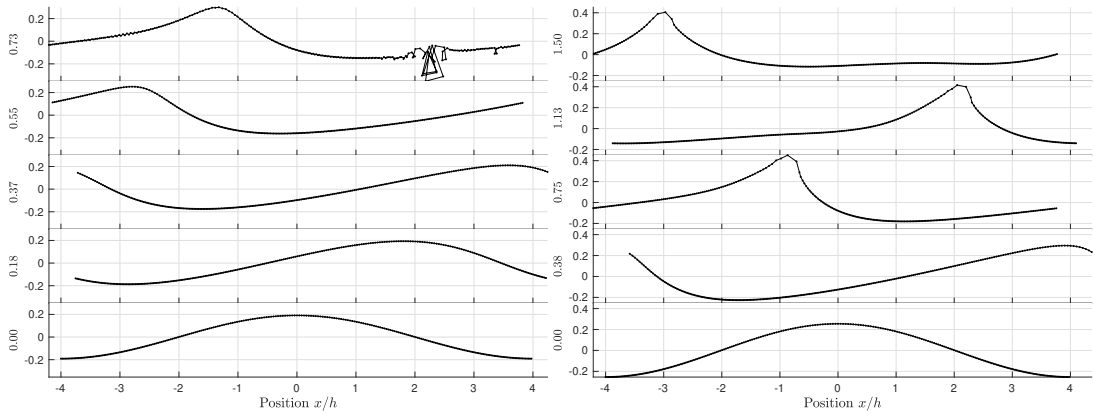
To explore the effects of modal damping, we compare passive stabilization with excessive damping. Without damping, high-wavenumber energy accumulates over time, eventually leading to numerical instability, as shown in [Figure 2a](#). Only a minimal amount of damping ($k_d = 0.50 k_{\max}$ and $r = 0.025$) is sufficient to permanently stabilise this case. This damping occurs at a scale and magnitude that do not affect wave dynamics. In contrast, the other panels of [Figure 2](#) illustrate cases where damping extends into active wave scales: In panel (b), damping is intensified and extended to the scale of the wave front, preventing overtopping and suppressing wave breaking, thus avoiding simulation failure. Panels (c) and (d) show an even larger wave, stabilised in panel (c) by broad-banded damping (small k_d), and in panel (d) by high-intensity damping (large r). The former causes a broader smearing of the wave crest, while an artificial crest ‘bubble’ forms in the latter. The bubble’s length scale is determined by k_d and resolution, and its formation appears to generate some secondary waves at similar scales. While (25) effectively maintains numerical stability, it does not constitute a physically realistic wave-breaking model. Developing a dedicated wave breaking model remains an important direction for future work.

Anti-aliasing measures are also a common feature of spectral methods, addressing resolution errors that arise when nonlinear operations are performed on discrete variables in physical space. This causes high-wavenumber energy to fold back onto lower wavenumbers. To mitigate the issue, anti-aliasing involves padding inputs to the inverse Fourier transform, ensuring sufficient resolution in physical space to prevent energy folding ([West et al., 1987](#)). The padding that absorbed the trickle down of energy is then removed at the next Fourier transformation. Since the conformal mapping model involves operations of division we cannot formally eliminate aliasing errors. However, [Chalikov and Sheinin \(2005\)](#) observed that simulations become insensitive to additional padding beyond cubic nonlinearity (i.e., adding zero-modes above wavenumber $3 k_{\max}$). Furthermore, it is the authors experience that aliasing errors rarely impact short-duration simulations like those presented here. Nevertheless, sensitivity should be checked, and anti-aliasing measures included when studying longer wave field evolutions.

Wave absorption is also often needed when simulating closed environments such as wave tanks. This is usually achieved by including a ‘numerical beach’ into the model, which can either be intended to reproduce the reflection of an actual beach, or just to emulate a radiating boundary. An approximate variant of the absorption layer method of [Bonnetfoy et al. \(2010\)](#) is implemented in the author’s code, setting

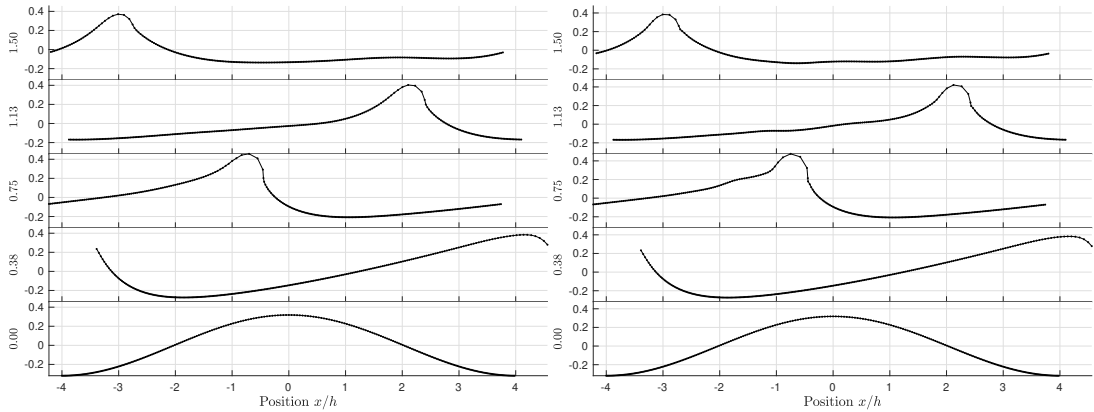
$$\bar{\bar{\phi}}_t := \bar{\phi}_t - \bar{v}(\bar{x})y_t^s, \quad y_t^s \approx \text{Im} \left(\bar{f}_t + \bar{f}_{\bar{z}}\bar{f}_t \right), \quad \nu = \nu_0 u^2 (3 - 2u); \quad u = \max(x - x_b, 0)/L_b, \quad (26)$$

absorption intensity ν_0 and beach length L_b suitably chosen.



(a) Non-breaking wave without stabilisation, $ka = 0.15$.

(b) Wave breaking suppressed by damping; $ka = 0.20$, $k_d = 0.25 k_{\max}$, $r = 0.10$.



(c) Strong wave breaking suppressed by wide-banded damping; $ka = 0.25$, $k_d = 0.10 k_{\max}$, $r = 0.10$.

(d) Strong wave breaking suppressed by high-intensity damping; $ka = 0.25$, $k_d = 0.25 k_{\max}$, $r = 0.50$.

Figure 2: Impact of excessive stabilisation coefficients on wave dynamics. All examples are initiated with a single-period linear wave at water depth $kh = \pi/4$. Very slight damping is sufficient to stabilise the case in panel (a).

3 The mapping function $\bar{f}(\bar{z}, t)$

The intermediate mapping function $\bar{f}(\bar{z}, t)$ maps the bathymetry to a horizontal line at constant depth $\bar{z} = \bar{x} - i\bar{h}$, and walls, if present, onto stationary vertical lines $\bar{z} = \bar{x}_1^w + i\bar{y}$ and $\bar{z} = \bar{x}_2^w + i\bar{y}$. Whenever permissible, we also map the still water line $z = x$ onto $\bar{z} = \bar{x}$ such that the x-axis of the two planes align. This alignment is beneficial for orientation and potentially also stability, but is not a requirement. We will in this section explore two families of such map functions and also demonstrate the mapping of a piston wavemaker.

3.1 An analytical bathymetry step

The Schwartz–Christoffel theorem (e.g., [Milne-Thomson, 1962](#), §10.2) is a powerful tool constructing mappings with straight-line boundaries and sharp angles. The theorem

provides the derivative $\bar{f}_{\bar{z}}$ of a function that bends the bathymetry line abruptly with prescribed angles at prescribed locations. When applied directly to a rectangular step, the theorem yields $\bar{f}_{\bar{z}} \propto \sqrt{\bar{z}+1}/\sqrt{\bar{z}-1}$, which can be integrated to match a step bathymetry transition from a shallower depth h_1 and deeper depth h_2 :

$$\bar{f}(\bar{z}) = \frac{h_2 - h_1}{\pi} (\sqrt{\bar{z}+1}\sqrt{\bar{z}-1} + \operatorname{arccosh} \bar{z}) - i h_2, \quad \operatorname{Im} \bar{z} \geq 0. \quad (27)$$

However, this map curves along the real axis and continues to do so far away from the step. To achieve a better mapping—one that remains flat along $y = 0$ through compression and quickly resumes a Cartesian shape—we turn to the textbook example of flow in an abruptly expanding channel (Milne-Thomson, 1962, §10.7). The trick of this solution is modelling the flow field using a source placed at infinity, and we here regard this flow field as itself being a coordinate map, yielding

$$\bar{f}_{\bar{z}} = \frac{h_1}{\pi\tau}, \quad \tau = \sqrt{\frac{\exp(\bar{z}) + c^2}{\exp(\bar{z}) + 1}}, \quad (28)$$

with constant $c = h_2/h_1$. Remarkably, the map is also analytically integrable:⁴

$$\bar{f}(\bar{z}, t) = -i h_1 + \frac{h_2}{\pi} \left[\frac{1}{c} \ln^+ \frac{\tau - c}{\tau + c} - \ln \frac{\tau - 1}{\tau + 1} \right]. \quad (29)$$

The area from the still water level to the floor is thus mapped into the logarithmic strip $-\pi \leq \bar{y} \leq 0$ and mirrored for $0 < \bar{y} < \pi$. Consequently, we have $\bar{h} = \pi$. An example is shown in Figure 3. Notably, the still water line $y = 0$ aligns with $\bar{y} = 0$ in the \bar{z} -plane and that coordinates are compressed on the shallow side. The direction of the step is reversed by flipping the abscissa $z = -\bar{f}(-\bar{z})$, and we can of course map sequences of steps using (29) provided these are far enough apart to avoid curvature at the seams.

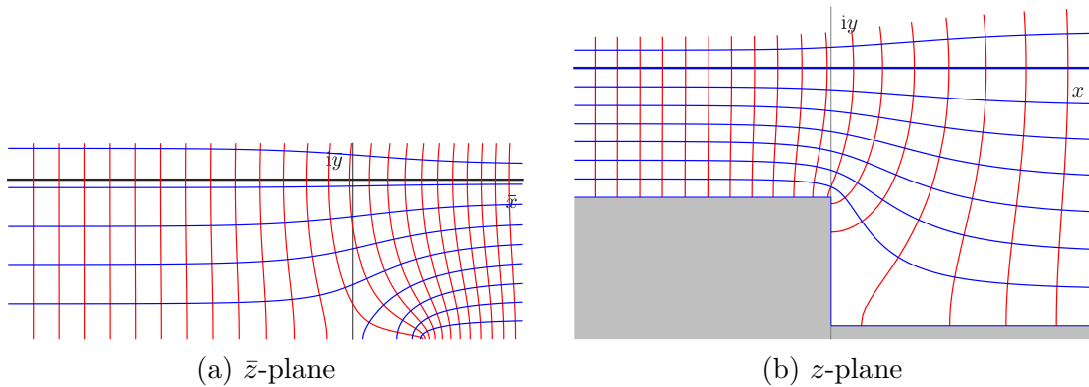


Figure 3: A step mapped with adjusted Schwarz–Christoffel transform (29)

⁴The correct logarithm branches must be chosen for the transition into $y > 0$ and so we introduce \ln^+ whose branch cut runs along 0 and 2π .

3.2 Compressed Schwartz–Christoffel maps using numerical integration

When analytical integration fails, numerical integration provides a straightforward alternative

$$\bar{f}(\bar{z} + \Delta\bar{z}) \simeq \bar{f}(\bar{z}) + \bar{f}'_{\bar{z}}(\bar{z} + \Delta\bar{z}/2) \Delta\bar{z}$$

where we are free to choose the integration path that best suits our mapping. Doing so, expression (28) can be generalised to accommodate an arbitrary number of angled planes with the expression

$$\bar{f}'_{\bar{z}}(\bar{z}, t) = \frac{h_1}{\pi} \prod_{j=1}^J [\exp(\bar{z} - \bar{\xi}_j) + 1]^{-\theta_j/\pi}; \quad \sum_{j=1}^J \theta_j = 0, \quad (30)$$

where outer angles $\{\theta_j\}$ are as observed in the z -plane, located at coordinates mapped from $\bar{z} = \bar{\xi}_j - i\pi$. A corner location will be a root of this expression when the corner is expanding ($\theta_j < 0$) and a singularity when the corner is contracting ($\theta_j > 0$). Expression (30) can also be written in the form $\bar{f}'_{\bar{z}}(\bar{z}, t) = \frac{h_1}{\pi} \prod_{j=1}^J (e^{\bar{z}} + e^{\bar{\xi}_j})^{\theta_j/\pi}$ which more closely resembles the original Schwartz–Christoffel theorem.

The asymptotic limits of $\bar{f}'_{\bar{z}}(\bar{z}, t)$ are

$$\lim_{\bar{x} \rightarrow -\infty} \bar{f}'_{\bar{z}}(\bar{z}, t) = h_1/\pi \quad \text{and} \quad \lim_{\bar{x} \rightarrow +\infty} \bar{f}'_{\bar{z}}(\bar{z}, t) = h_J/\pi, \quad (31)$$

h_1 and

$$h_J = h_1 \exp\left(\sum_{j=1}^J \frac{\bar{\xi}_j \theta_j}{\pi}\right) \quad (32)$$

respectively being the water depths found to the left and right of the combined bundle of corners. We can in other words a priori select $\{\bar{\xi}_j\}$ and $\{\theta_j\}$ to get the desired set of slopes and the desired outer water depths. For instance, a bathymetry with a single (outer) slope angle θ , transitioning from depth h_1 to h_2 , is obtained by numerically integrating

$$\bar{f}'_{\bar{z}}(\bar{z}, t) = \frac{h_2}{\pi} \left(\frac{\exp \bar{z} + 1}{\exp \bar{z} + (h_2/h_1)^{-\pi/\theta}} \right)^{-\theta/\pi}. \quad (33)$$

Of course, setting $\theta = -\pi/2$ recovers (28). An example of a slanting step is shown in Figure 4 with $\theta = -\pi/4$. If additional bathymetry angles are required at prescribed water depths, iteration on $\{\bar{\xi}_j\}$ is necessary. Examples of such geometries are presented in Figure 5, showing two slender protruding structures integrated using (30). The pressure and velocity field for a wave passing above the latter geometry is included in Figure 6. We note the peculiar feature of potential flows, that singularities of pressure and velocity appear at expanding corners, whereas contracting corners exhibit stagnation points. This poses no significant challenge computationally, and one can, if preferred, round the corners slightly by intentionally setting $\bar{h} < \pi$.

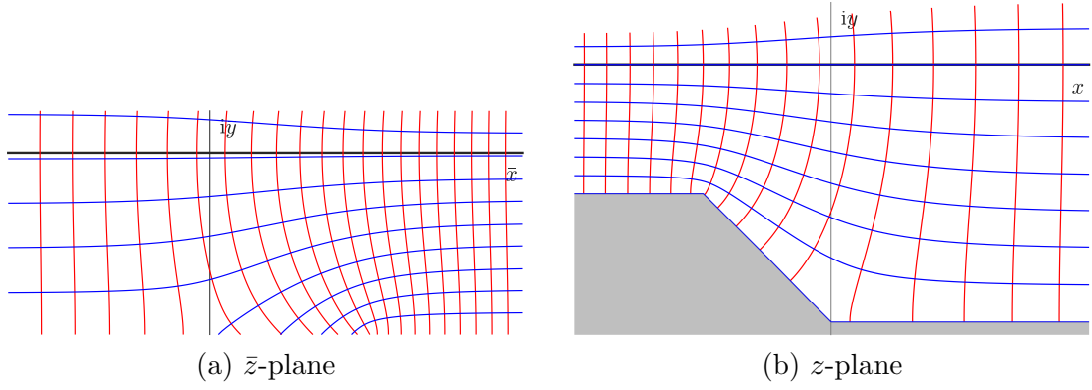


Figure 4: Numerical integration of (33) with $\theta = -\pi/4$, $h_1 = 0.5$, $h_2 = 1.0$.

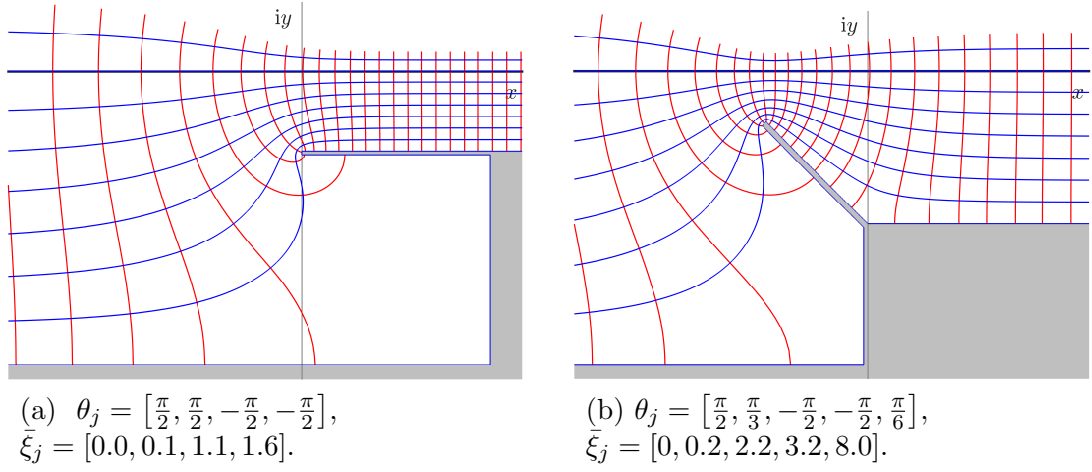


Figure 5: Example maps in z -plane constructed using (30).

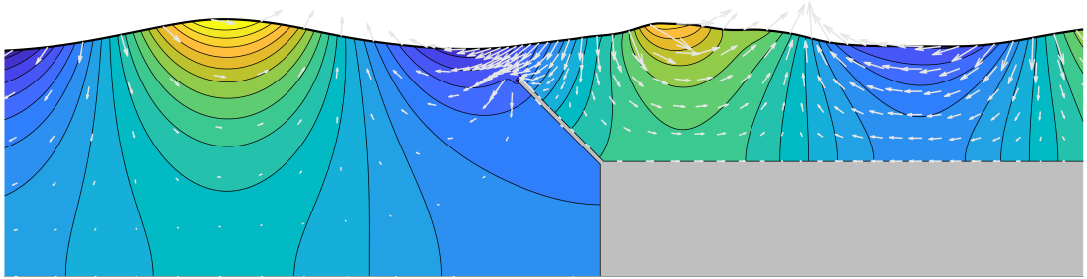


Figure 6: Simulation snapshot showing a regular wave interacting with the geometry in Figure 5b. The wave is visibly disturbed by the protruding structure. Contours represent dynamic pressure (22), and arrows indicate the velocity field. Arrows near the protruding tip have been omitted for clarity. Initial conditions: wave packet with steepness $kH/2 = 0.15$ and water depth $kh_1 = 3.0$.

3.3 Arbitrary smooth bathymetries

The projection kernels \mathcal{C} and \mathcal{S} in [Appendix A](#) serve as fundamental components of the present model. Similar to the free surface, these kernels allow for mapping of the bathymetry, provided it is sufficient smooth. This is achieved by introducing a z -plane depth function $H(x, t)$ defined as $\partial\mathcal{Z}^b(t) = \{x - iH(x, t)\}$, along with an equivalent \bar{z} -plane function $\bar{H}(\bar{x}, t)$ that takes the same values as $H(x, t)$ but with \bar{x} as argument. The mapping is then expressed as

$$\bar{f}(\bar{x}, t) = \bar{z} + i\bar{h} - i [\mathcal{S}_{-\bar{h}} * \bar{H}] (\bar{z} + i\bar{h}); \quad \bar{h} = \langle \bar{H} \rangle. \quad (34)$$

A quick iteration is necessary to precisely match a prescribed bathymetry because \bar{H} is function of \bar{x} rather than x . Since only the horizontal coordinates differ, a fixed-point iteration is usually sufficient—an example is provided in [Listing 2](#) and demonstrated in [Figure 7](#). The method performs well with smooth surfaces ([Figure 7b](#)) but fails when sharp angles are present ([Figure 7c](#)). Fortunately, for such cases, the approach outlined in [subsection 3.2](#) is highly effective.

The iterations in [Listing 2](#) can also be adopted to define the initial conditions of $\bar{\eta}$ and $\bar{\phi}^s$ in the \bar{z} -plane.

```
HH = H; xx = x;
for i = 1:n
    xMap = xx + imag(convKernel('S', -mean(HH), HH, xx, 0));
    HH = interp1(x, H, xMap);
end
```

Listing 2: Implementation example (MATLAB syntax) of iteration loop that determines $\bar{H}(\bar{x})$ precisely according to a prescribed bathymetry $H(x)$. The full map is then given by (34). The function `convKernel` is found in [Listing 3](#). Function `interp1` performs a linear interpolation.

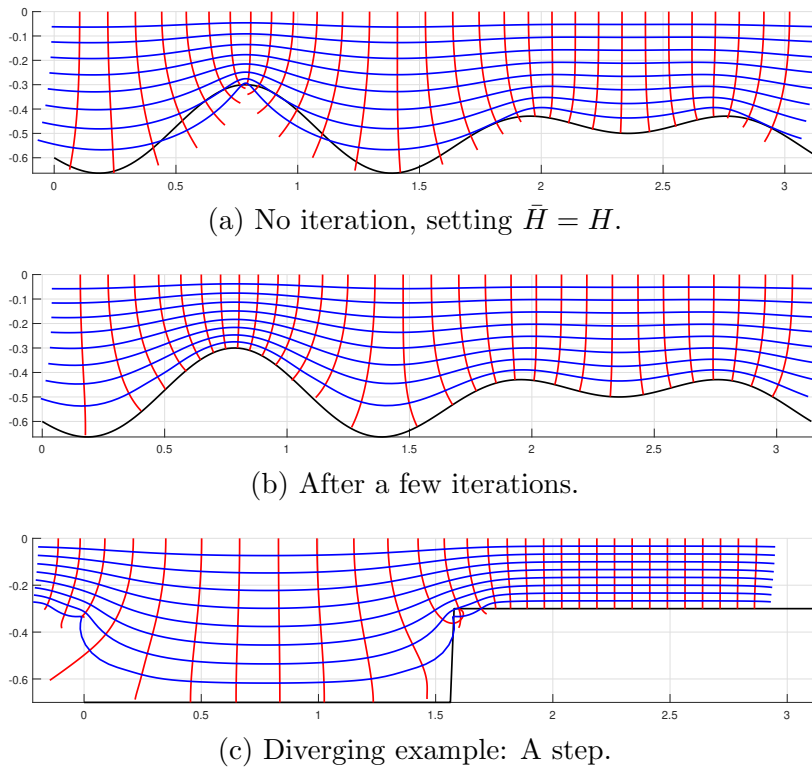


Figure 7: Bathymetry maps \bar{f} from (34) with iteration procedure exemplified in Listing 2. Target profile is $H(x) = .5 + .1(\cos 4x + \sin 6x)$. Also shown is a diverging example of a sharp step.

3.4 A piston wavemaker

Representing a piston wavemaker is remarkably straightforward with the present method—take a walled rectangular domain and shake it horizontally:

$$\bar{f}(\bar{z}, t) = \bar{z} + X(t); \quad X(t) \in \mathbb{R}. \quad (35)$$

The kinematic condition (6b) then leads to

$$\bar{W}_{\bar{z}} = X_t, \quad (36)$$

and equation (11) reduces to

$$\bar{\mu}^b = 0, \quad \bar{\mu}^s = \frac{\bar{\phi}_{\bar{y}}}{|\bar{f}_{\bar{z}}|^2} \Big|_{\bar{y}=0} \quad (37)$$

which completes the piston wavemaker model. The dimensions of the \bar{z} -plane remain the same as those in the z -plane, with $\bar{L} = L$ and $\bar{h} = h$.

Since we shake the entire domain, an identical wavemaker will generate waves at opposite phase at the opposite wall. These waves can be suppressed using a numerical beach, such as (26). Alternatively, movement of the right boundary can be avoided by replacing the translating map with one that expands and contracts:

$$\bar{f}(\bar{z}, t) = \bar{z} + \left(1 - \frac{\bar{z} + i\bar{h}}{\bar{L}}\right) X(t); \quad X(t) \in \mathbb{R}, \quad (38)$$

where $\bar{h} = h$ and \bar{L} equalling the wave tank length L when the wavemaker is in its neutral position $X = 0$. This map pulsates about the point $z = \bar{L} - ih$ with an expansion factor

$$\alpha(t) = 1 - \frac{X(t)}{\bar{L}} = \bar{f}_{\bar{z}}. \quad (39)$$

The background velocity, satisfying (6b), is then given by

$$\bar{W}_{\bar{z}} = \left(1 - \frac{\bar{z} + i\bar{h}}{\bar{L}}\right) \alpha X_t \quad (40)$$

which enters the surface boundary condition but not the bottom condition where $\text{Im } \bar{W}_{\bar{z}} = 0$:

$$\bar{\mu}^b = 0, \quad \bar{\mu}^s = \left[\frac{\bar{\phi}_{\bar{y}}}{\alpha^2 |\bar{f}_{\bar{z}}|^2} + 2 \frac{\bar{y} + \bar{h} \text{Re } \bar{f}_{\bar{z}}}{\alpha \bar{L} |\bar{f}_{\bar{z}}|^2} X_t \right]_{\bar{y}=0}. \quad (41)$$

Note that $y = 0$ no longer maps to $\bar{y} = 0$ but rather to $\bar{y} = \bar{h}X/\alpha\bar{L}$. A comparison between map (35) and (38) is provided later, in Figure 13.

4 Simulation examples and validation

4.1 Steep waves on flat bathymetry (validation)

As mentioned earlier, conformal mapping is particularly advantageous in shallow waters, and so shallow water Stokes waves are considered in our first benchmark. Figure 8 shows the surface elevation of such waves in space and time, and compares their progression to the phase velocity computed with the SSGW algorithm of Clamond and Dutykh (2018). The initial surface elevation and potential are taken from this reference, and five wave crests are simulated over five periods in a periodic domain, requiring about two CPU seconds. The waves maintain their shape and propagate with expected celerity (red line).

HOS methods are powerful tools for intermediate water depths and three-dimensional wave fields. Accuracy and efficiency are however closely tied to the required order of HOS nonlinearity, M_{nl} , the number of FFT operation per time step being $4 + M_{\text{nl}}(M_{\text{nl}} + 3)/2$, plus an additional four for filtering. Repeating the previous simulation (five waves, five periods, $kh = 0.5$) for varying wave steepness produces the surface profiles shown in Figure 9. A nonlinearity order of three accurately captures the moderately steep wave $kH/2 = 0.05$, while orders between five and ten are needed for $kH/2 = 0.10$. The steepest wave, $kH/2 = 0.15$, converges almost but not quite with 15 orders and diverges beyond that. Various HOS method versions exist today, and alternative initial conditions—such as gradually increasing model nonlinearity over time—may yield better results. Nevertheless, this example highlights the inherent advantage of the conformal mapping method over the HOS model in shallow waters. Conformal mapping requires seven FFT transformations per time step, plus an additional four for the stabilisation (24).

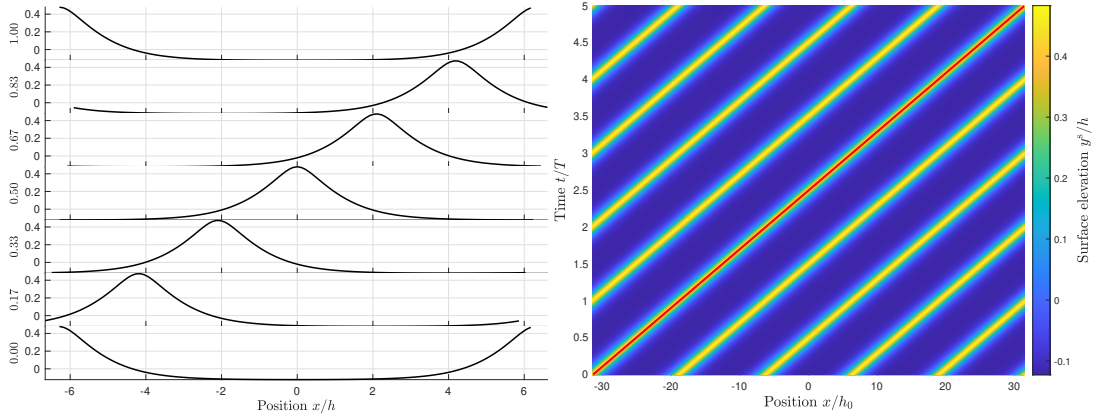


Figure 8: Surface elevation of a shallow water Stokes wave initiated from SSGW. Red line in left panel shows the phase velocity predicted by SSGW. Steepness $kH/2 = 0.15$, water depth $kh = 0.5$.

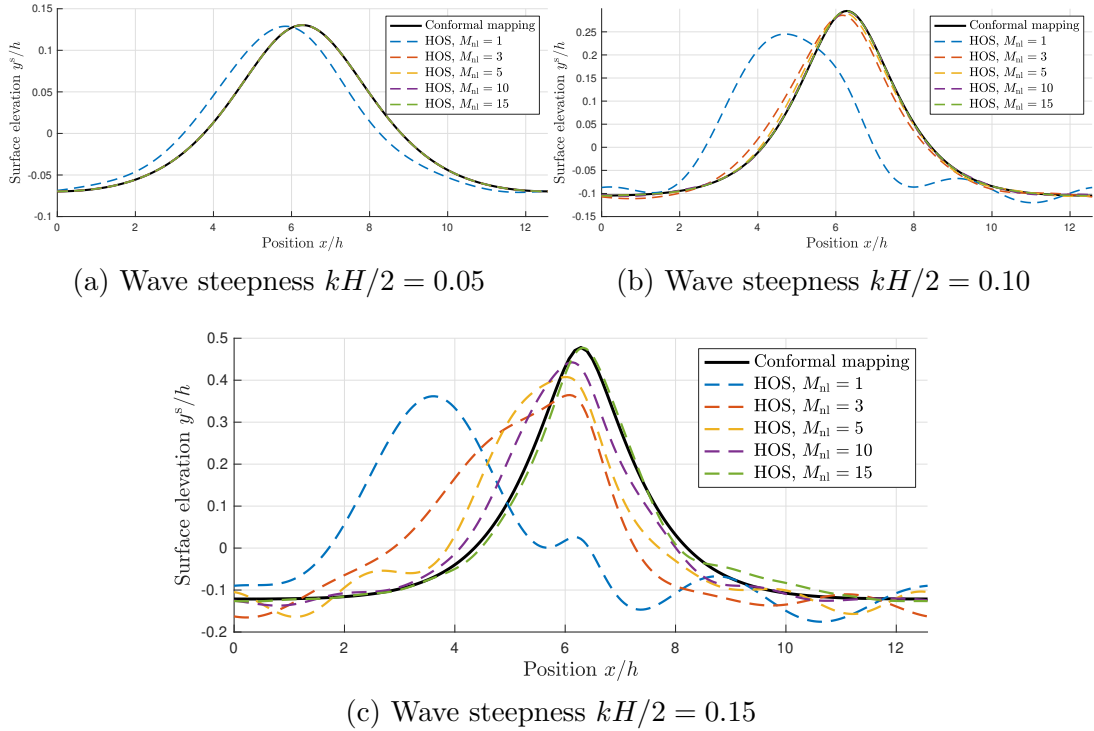


Figure 9: Comparison to simulations with the HOS method at various orders of non-linearity M_{nl} ; surface elevation after simulating five wavelengths for five periods, cf. Figure 8. Initial state generated with SSGW. Water depth $kh = 0.5$.

While considering flat bathymetries, it is natural to reproduce one of the more striking cases presented by Chalikov and Sheinin (2005). Figure 10 captures a snapshot from a simulation whose initial conditions were that of an extremely steep linear wave crest ($ka = 0.5$) within a periodic domain. Shortly after initiation, the wave breaks, and the snapshot is taken just before the simulation crashes. Our essentially parametric surface description permits a slight folding of the wave crest. However, the dynamics of

the plunging wave front cannot be captured within the framework of potential theory. The contours in [Figure 10](#) display, for comparison to reference, the ‘deviation from the generalised hydrostatic pressure’, whose difference from the dynamic pressure is $g\bar{y} - gy$. Consistent with our reference, we observe the same pressure ‘bubble’ underneath the wave front. The water depth of this case is $kh = \pi$, with stabilisation parameters $k_d = 0.5 k_{\max}$ and $r = 0.25$, using a padding factor of 4.5.

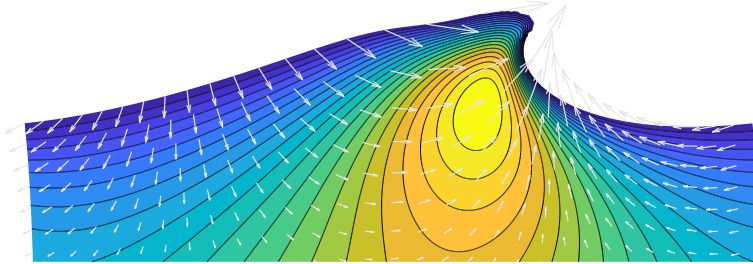


Figure 10: Breaking wave case corresponding to figure 2 in [Chalikov and Sheinin \(2005\)](#). Contours show deviation from the generalised hydrostatic pressure $p + g\bar{y}$. (Image tapered from below.)

4.2 Piston wavemaker (map of [subsection 3.4](#))

The simple mapping described in [subsection 3.4](#) enables arbitrary wavemaker motions, typically composed of random Fourier components distributed according to an energy spectrum. For testing purposes, we consider a single-harmonic wavemaker motion, $X_0(t) = \hat{X}_0 \sin \omega_0 t$, with an added ramp $R(t)$ to softens the initial motion: $X(t) = X_0(t)R(t)$, $X_t = \mathcal{F}^{-1} [i\omega \mathcal{F}(X_0 R)]$, and so forth.

First, we verify the boundary conditions. As shown in [Figure 11](#), the condition $\phi_x[X(t), y, t] = X_t(t)$ is exactly satisfied per map design. Vertical velocities in the mid water depth range are also shown in the figure.

The surface elevation for this case is the depicted in [Figure 12](#), along with a validation comparison against one of SINTEF Ocean’s in-house codes. This in-house model is a sigma-grid-based FEM [Wu and Taylor \(1995\)](#), incorporating Lagrangian particle support. It has, in turn, been benchmarked against other FDM codes. The agreement in [Figure 12](#) is excellent but for a slight difference in phase velocity as seen at the front end of the wave train. This discrepancy originates in fact from grid stretching errors in the reference model—a well documented limitation of sigma-grid transformations. Grid stretching error can be minimised through clever meshing ([Pakozdi et al., 2021](#)) given prior knowledge of phase velocity.

The wavemaker example highlights the core challenge of wave generation: a single-harmonic wavemaker motion inevitably produces spurious super-harmonic waves alongside the primary wave. These propagate at slower group velocities and are therefore observed at the back end of the wave train, leaving the front end unaffected. These will, as seen in the figure, propagate at slower group velocities. Wave contamination is therefore observed at the back-end of the wave train, leaving the front-end clean. To further emphasise this effect, a second case with double the piston stroke is included in [Figure 12](#), shown in a dot-dashed line. The simulations run in a few seconds, whereas the FEM/FDM codes require several orders of magnitude more computation time.

Both wavemaker mappings introduced in [subsection 3.4](#) yield the results shown,

which display only the region near the wavemaker. The difference between the mappings become evident when zooming out, as in Figure 13, to include the beach-side section of the wave tank. With mapping (35), waves of opposite in phase and direction are being generated at the beach end of the domain. No beach-side wave generation occurs with mapping (38).

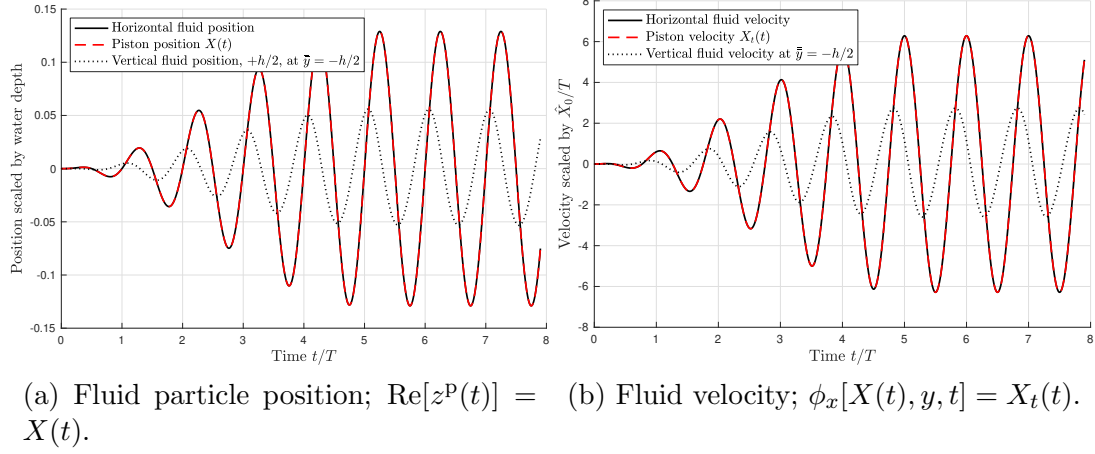


Figure 11: Validation of the piston boundary condition.

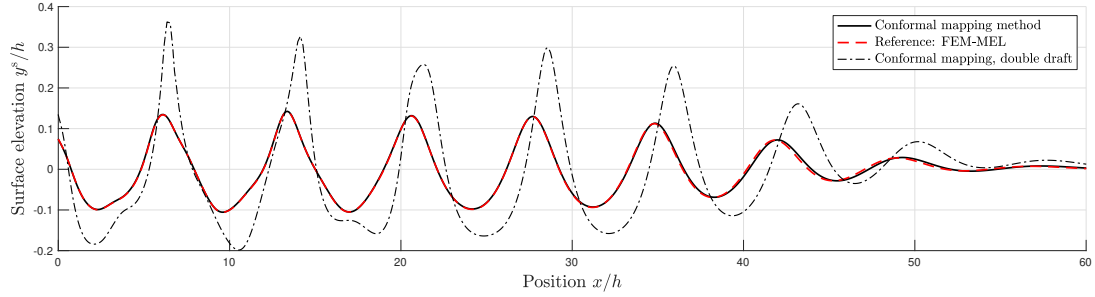


Figure 12: Validation of simulated surface elevation against. The period is $T = 7.93\sqrt{h/g}$.

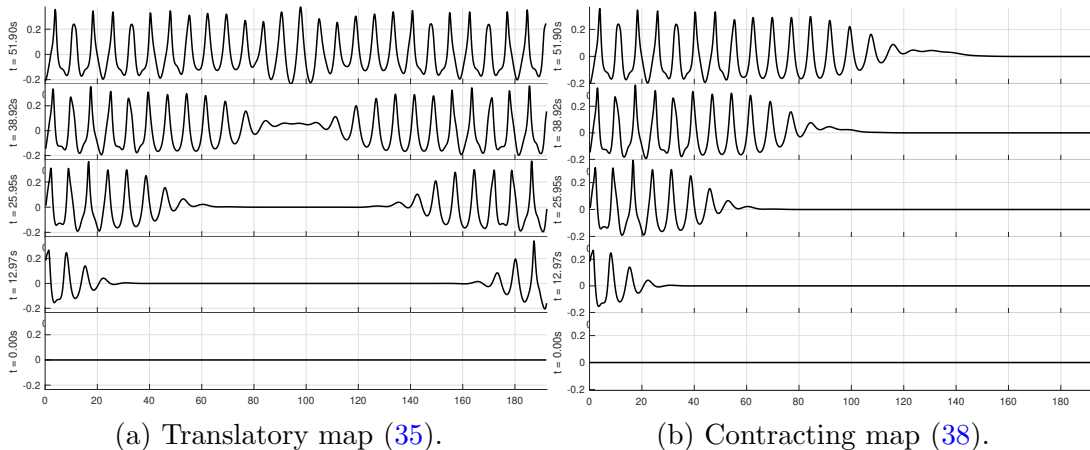


Figure 13: Full domain simulated in above figures, comparing the two wavemaker maps in subsection 3.4. Case with double piston draft. No numerical beach included.

4.3 A tsunami (map of subsection 3.1)

We now turn to testing transient bathymetries selecting the case of a tsunami triggered by the uplift of a tectonic shelf, modelled using the analytically integrated map (29). The initially flat shelf rises during a transition period T_f until reaching a final height Δh . For ease of validation, the rise velocity is made constant.

Map (29) is applied for this test, with time dependency introduced by defining $h_1(t) = h_2 - \Delta h \min(t/T_f, 1)$. The time derivative is computed using discrete differentiation $\bar{f}_t = [\bar{f}(\bar{z}, t + \epsilon/2) - \bar{f}(\bar{z}, t - \epsilon/2)]/\epsilon$. The mirroring approach (8) is applied to the lateral boundaries, but without an added background potential. This enforces zero horizontal velocity along lateral boundaries, even as the left boundary shifts in time. The boundary then remains stable and does not interfere with the simulation, provided wave never reach the domain edges.

We again start by verifying the kinematic boundary conditions, this time at the bed. Figure 14 presents the velocity field w_z^* for a representative case. As required, the vertical velocity remains zero in the right half of the domain, while in the left half, it equals the shelf rise velocity $\Delta h/T_f$ during the transition period T_f , returning to zero afterwards. The left boundary also shifts rightward as the shelf rises, due to coordinate compression in this region. This reduces the length of the domain but causes no other issues. If preferred, the shift can be greatly reduced by choosing a mapping function which, instead of compressing the left domain, rises it. A suitable alternative is the simpler Schwartz–Christoffel step transformation (27).

Figure 15 illustrates surface elevations for varying values of Δh and T_f . The solutions exhibit a far-field plateau that follows the bathymetric rise. In between, an intermediate plateau fans out, connecting to the far fields through a rarefaction wave and a softened shock front. Waves generated by transient dynamics occupy this middle plateau. These form secondary wave fronts when the shelf rises abruptly.

Snapshots of the interior velocity field are shown in Figure 16 for the most abrupt rise. Field recreation uses (12) and (15), requiring only the prescribed mapping function and surface variables $\bar{\eta}$ and $\bar{\phi}^s$. As with previous cases, computation time remains within the scale of seconds, depending on resolution and the intensity of transients.

The dynamic ODE solver adopts fine time stepping during the depth transition and then quickly speeds up once the bed reaches its stationary state.

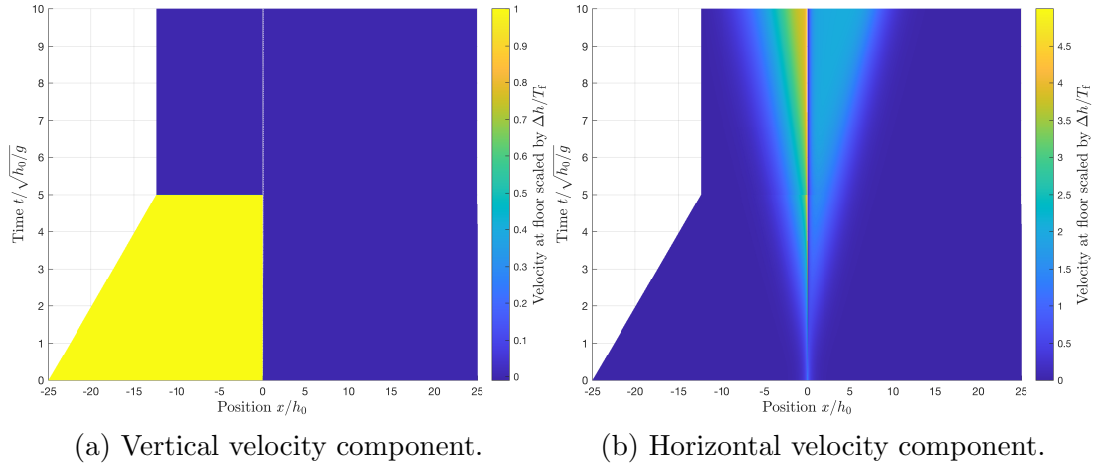
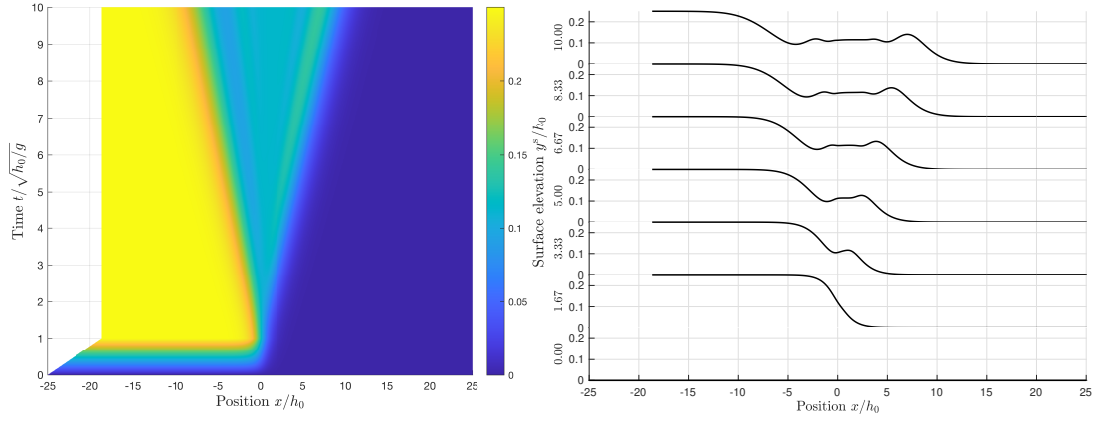
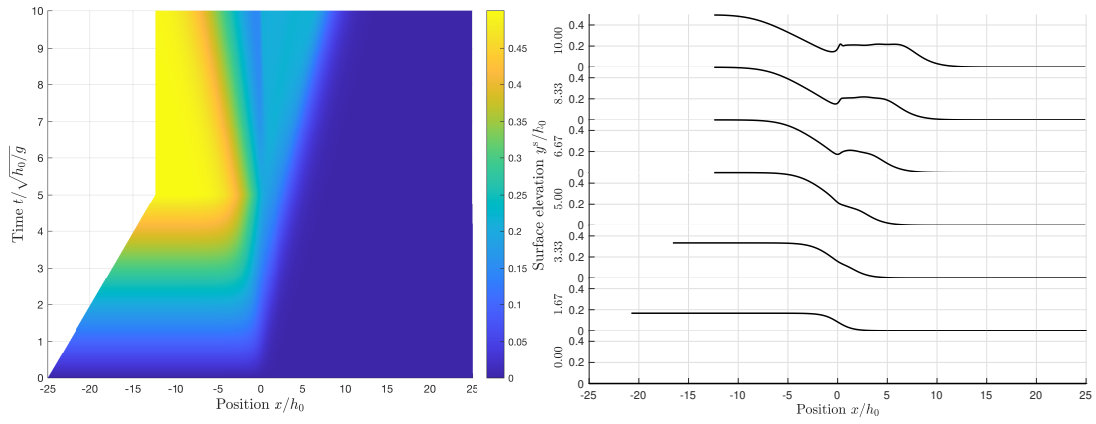


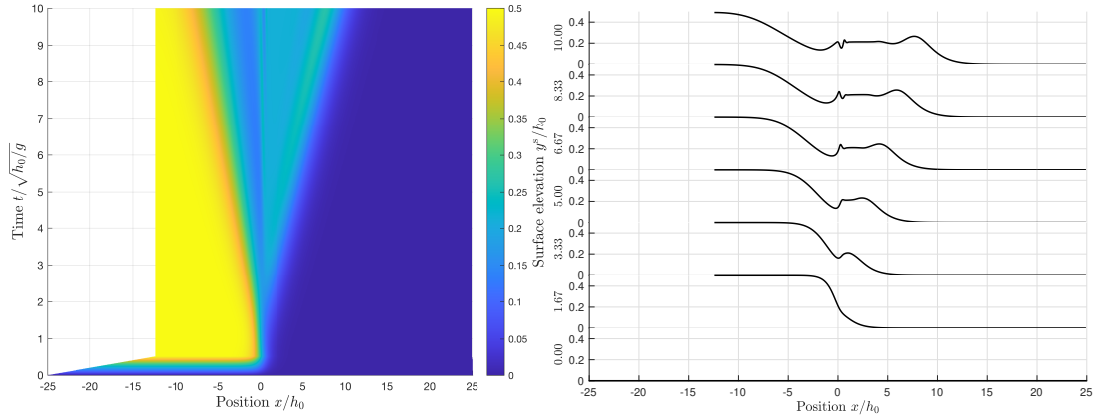
Figure 14: Velocity at bed, scaled by the prescribed shelf rise speed $\Delta h/T_f$. $\Delta h = 0.50 h_0$, $T_f = 10.0\sqrt{h_0/g}$.



(a) Light case; $\Delta h = 0.25 h_0$, $T_f = 1.0\sqrt{h_0/g}$.



(b) Slow case; $\Delta h = 0.50 h_0$, $T_f = 10.0\sqrt{h_0/g}$.



(c) Abrupt case; $\Delta h = 0.50 h_0$, $T_f = 0.5\sqrt{h_0/g}$.

Figure 15: Tsunami example; surface elevation caused by a bottom shelf rising at fixed velocity $\Delta h/T_f$ during a period T_f .

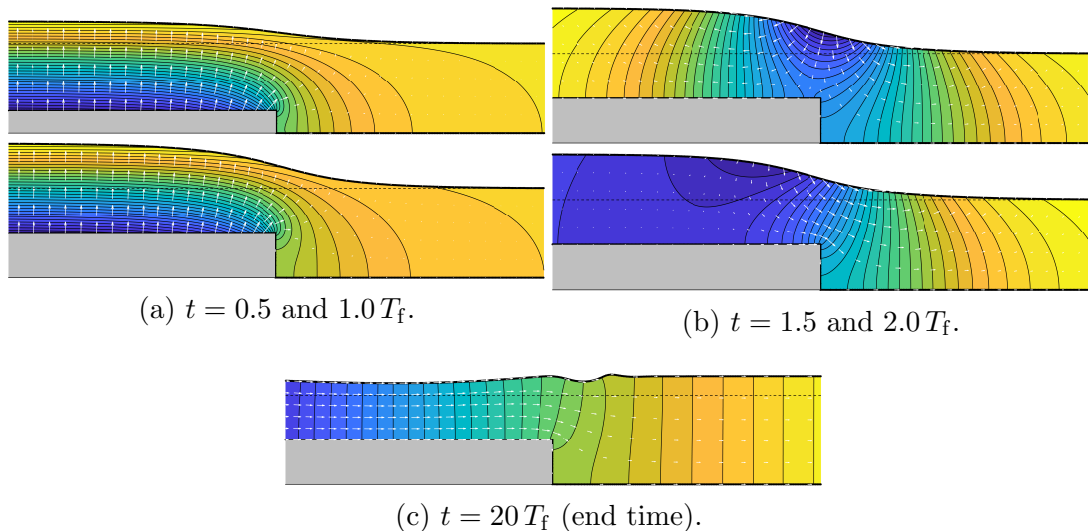


Figure 16: Velocity and potential field reconstructed from surface variables. Abrupt rise case shown in [Figure 15c](#)

4.4 Wave reflection across a depth transition ramp (map of [subsection 3.2](#))

As a final example, a small study made at SINTEF Ocean in Norway is briefly reproduced. The study was part of the design process for the Norwegian Ocean Technology Centre, which is currently under construction. It investigated whether installing a beak-shaped extension at the edge of an abrupt depth transition could reduce wave reflections; two geometry examples are shown in [Figure 17](#). Simulations were performed using the prototype model (23), varying beak angles and deep-side water depths while keeping the beak length and shallow-side depth fixed. Short wave packets were initialised and allowed to propagate across the depth transition. Having passed the transition, all the wave energy that remains on the deep-water side is assumed to be reflected energy. Integrating this, reflection coefficient

$$C_r(t) = \left\{ \int_{-\infty}^0 [y^s(x, t)]^2 dx / \int_{-\infty}^0 [y^s(x, 0)]^2 dx \right\}^{1/2} \quad (42)$$

is computed. [Figure 18](#) illustrates the process and the evolution of $C_r(t)$ over time as the packet transitions. A final reflection value was determined as the filtered minimum of $C_r(t)$. The process was easily automated, enabling rapid generation of the reflection chart in [Figure 19](#). Each simulation required about 30 to 60 CPU seconds, with a full reflection curve computed in 10 to 20 minutes. The study confirmed that the beak extension reduces reflection, with an optimal beak angle that depends on the water depth—approximately 25° for a 12 meter depth and 20° for 7 meters.

A final benchmark is included in [Figure 19a](#); dotted black lines show the predictions from linear mode-matching theory (e.g., [Li et al., 2021](#)), which applies to straight step transitions $\theta = 90^\circ$. The reference model shows remarkable agreement, especially considering the simplicity of estimate (42). To avoid wave breaking, the initial wave steepness is a moderate $kH/2 = 0.05$ in all cases. Waves undergo significant steepening after the depth transition, increasingly so for larger periods. The release and reflection

of second-order bound harmonics are clearly seen in Figure 18a as secondary wave packets, while higher-order free wave packets become visible with increasing steepness. Better simulation performance and steeper waves can be obtained with the full conformal mapping model.

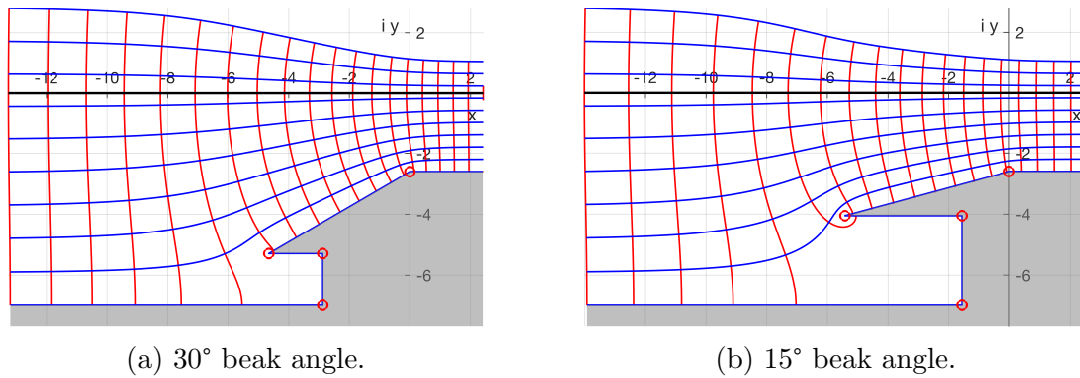


Figure 17: Beak geometry maps with a depth transition from 7.0 to 2.6 meters.

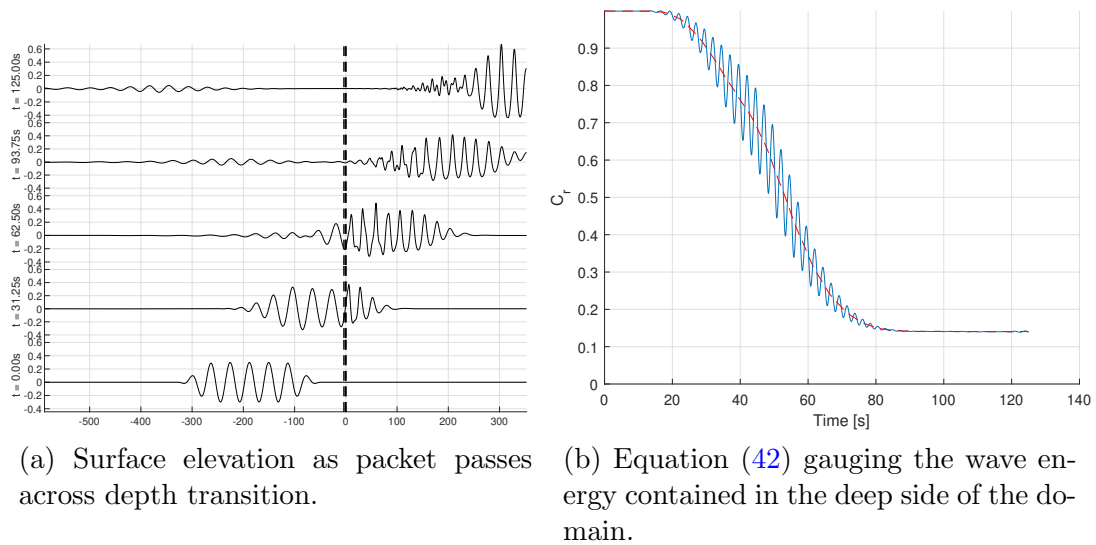


Figure 18: Illustration of analysis for example period 5.0 seconds, 45° beak angle, depth transition from 12.0 to 2.6 meters.

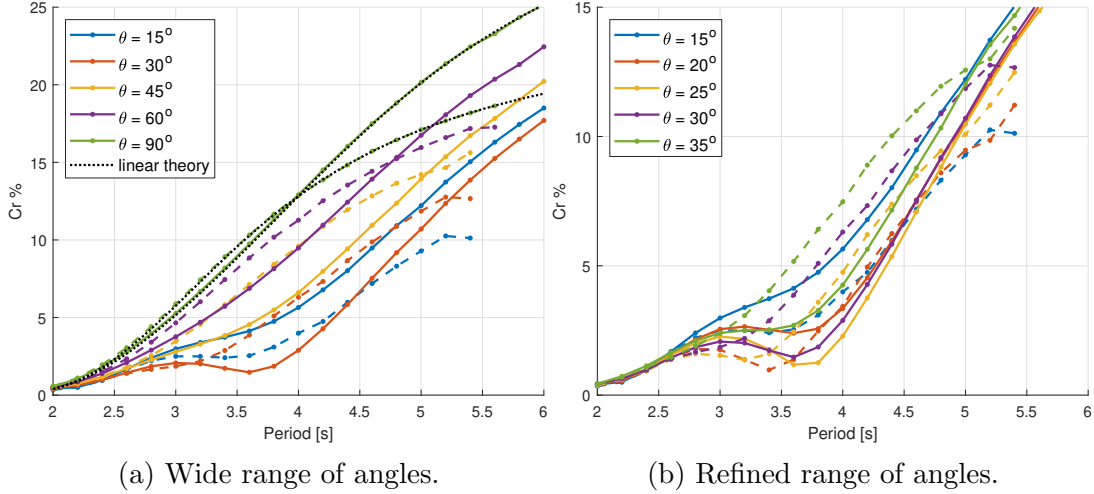


Figure 19: Reflection curves as function of wave period. Transition from two depths, 12.0 meters (solid lines) and 7.0 meters (dashed lines), are shown, shallow water depth being 2.6 meters. A reference estimate from linear theory for $\theta = 90^\circ$ is also included. Beak angles are displayed in the legend.

5 Closing remarks

A water wave simulation method based on conformal mapping has been presented, along with a range of practical examples. The method demonstrates high accuracy in all cases and never requires more than a minute of CPU time. At its core, the model simulation routine follows a compact series of explicit steps. Initialisation involves additional routines for setting initial conditions and mapping of the domain geometry, but these introduce negligible computational overhead. Efficiency is strongly dependent on resolution, wave steepness, the intensity of transients, numerical stabilisation and the extent of anti-aliasing, and so a more precise measure of efficiency has therefore not been pursued here.

Development of a wave breaking model within the conformal mapping framework is recommended. While dissipation model (24) effectively suppresses high-wavenumber energy buildup, it is ad hoc and should not be relied upon to represent the propagation and dissipation process of a breaking wave front. Instead, wave breaking models should be incorporated into the conformally mapped model, drawing from established studies on wave-breaking dynamics. [Seiffert et al. \(2017\)](#); [Seiffert and Ducrozet \(2018\)](#) have already successfully integrated such a model into the HOS scheme, using the breaking onset criterion of [Barthelemy et al. \(2018\)](#) and the eddy dissipation models of [Tian et al. \(2010\)](#). Conceptually, the detailed information about crest evolution curvature that is available in the conformal representation could be advantageously utilized in this respect.

Conformal mapping has great potential for wavemaker modelling and, to the author's knowledge, this represents the first wavemaker model of its kind. In addition to the piston-type wavemaker models presented here, the author has recently developed a paddle-type wavemaker models, which has been successfully validated. Due to its scope and potential impact, its details are reserved for a forthcoming paper that

builds upon the present study. The paddle wavemaker completes the conformal mapping model as a fully functional numerical wave tank, enabling integration with most wave generation systems.

Acknowledgements

The authors would like to acknowledge support from Statsbygg, the Norwegian Directorate of Public Construction and Property, as part of the Norwegian Ocean Technology Centre (NHTS) project which is currently under construction in Trondheim, Norway. Csaba Pákozdi at SINTEF Ocean has kindly supplied wavemaker benchmark data and the author is grateful to Kontorbamse for continued academic support.

References

- X. Barthelemy, M. L. Banner, W. L. Peirson, F. Fedele, M. Allis, and F. Dias. On a unified breaking onset threshold for gravity waves in deep and intermediate depth water. *Journal of Fluid Mechanics*, 841:463–488, 2018. doi: 10.1017/jfm.2018.93.
- F. Bonnefoy, D. Le Touzé, and P. Ferrant. A fully-spectral 3D time-domain model for second-order simulation of wavetank experiments. Part A: Formulation, implementation and numerical properties. *Applied Ocean Research*, 28(1):33–43, 2006.
- F. Bonnefoy, G. Ducrozet, D. Le Touzé, and P. Ferrant. Time domain simulation of nonlinear water waves using spectral methods. In *Advances in numerical simulation of nonlinear water waves*, pages 129–164. World Scientific, 2010.
- D. Chalikov. Numerical modeling of sea waves. *Izvestiya, Atmospheric and Oceanic Physics*, 56:312–323, 2020.
- D. Chalikov and A. V. Babanin. Three-dimensional periodic fully nonlinear potential waves. In *International Conference on Offshore Mechanics and Arctic Engineering*, volume 55331, page V02BT02A056. American Society of Mechanical Engineers, 2013.
- D. Chalikov and D. Sheinin. *Numerical modeling of surface waves based on principal equations of potential wave dynamics*. US Department of Commerce, National Oceanic and Atmospheric Administration National Weather Service, 1996.
- D. Chalikov and D. Sheinin. Modeling extreme waves based on equations of potential flow with a free surface. *Journal of Computational Physics*, 210(1):247–273, 2005.
- D. V. Chalikov. *Numerical modeling of sea waves*. Springer, 2016.
- D. Clamond and D. Dutykh. Fast accurate computation of the fully nonlinear solitary surface gravity waves. *Computers & fluids*, 84:35–38, 2013.
- D. Clamond and D. Dutykh. Accurate fast computation of steady two-dimensional surface gravity waves in arbitrary depth. *Journal of Fluid Mechanics*, 844:491–518, 2018.
- D. Clamond, D. Dutykh, and A. Durán. A plethora of generalised solitary gravity–capillary water waves. *Journal of Fluid Mechanics*, 784:664–680, 2015.

- F. Dias and J.-M. Vanden-Broeck. Open channel flows with submerged obstructions. *Journal of Fluid Mechanics*, 206:155–170, 1989.
- G. Ducrozet, F. Bonnefoy, D. Le Touzé, and P. Ferrant. HOS-ocean: Open-source solver for nonlinear waves in open ocean based on High-Order Spectral method. *Computer Physics Communications*, 203:245–254, 2016.
- G. Ducrozet, F. Bonnefoy, N. Mori, M. Fink, and A. Chabchoub. Experimental reconstruction of extreme sea waves by time reversal principle. *Journal of Fluid Mechanics*, 884:A20, 2020. doi: 10.1017/jfm.2019.939.
- D. Dutykh and D. Clamond. Efficient computation of steady solitary gravity waves. *Wave Motion*, 51(1):86–99, 2014.
- D. Dutykh, D. Clamond, and A. Durán. Efficient computation of capillary–gravity generalised solitary waves. *Wave Motion*, 65:1–16, 2016.
- L. K. Forbes and L. W. Schwartz. Free-surface flow over a semicircular obstruction. *Journal of Fluid Mechanics*, 114:299–314, 1982.
- M. Gouin, G. Ducrozet, and P. Ferrant. Development and validation of a nonlinear spectral model for water waves over variable depth. *European Journal of Mechanics – B/Fluids*, 57:115–128, 2016. ISSN 0997-7546. doi: <https://doi.org/10.1016/j.euromechflu.2015.12.004>. URL <https://www.sciencedirect.com/science/article/pii/S0997754615301394>.
- M. Gouin, G. Ducrozet, and P. Ferrant. Propagation of 3d nonlinear waves over an elliptical mound with a high-order spectral method. *European Journal of Mechanics – B/Fluids*, 63:9–24, 2017. ISSN 0997-7546. doi: <https://doi.org/10.1016/j.euromechflu.2017.01.002>. URL <https://www.sciencedirect.com/science/article/pii/S0997754616302795>.
- J. Hennig, J. Scharnke, C. Swan, Ø. Hagen, K. Ewans, P. Tromans, and G. Forristall. Effect of short-crestedness on extreme wave impact: A summary of findings from the joint industry project “shortcrest”. In *International Conference on Offshore Mechanics and Arctic Engineering*, volume 56499, page V003T02A047. American Society of Mechanical Engineers, 2015.
- H. Houtani, T. Waseda, W. Fujimoto, K. Kiyomatsu, and K. Tanizawa. Generation of a spatially periodic directional wave field in a rectangular wave basin based on higher-order spectral simulation. *Ocean Engineering*, 169:428–441, 2018.
- A. Khait and L. Shemer. Application of boundary element method for determination of the wavemaker driving signal. *Journal of Offshore Mechanics and Arctic Engineering*, 141(6):061102, 2019.
- H. Lamb. *Hydrodynamics*, 1932.
- Y. Li, Y. Zheng, Z. Lin, T. A. A. Adcock, and T. S. van den Bremer. Surface wavepackets subject to an abrupt depth change. part 1. second-order theory. *Journal of Fluid Mechanics*, 915:A71, 2021. doi: 10.1017/jfm.2021.48.

- M. McAllister, S. Draycott, R. Calvert, T. Davey, F. Dias, and T. van den Bremer. Three-dimensional wave breaking. *Nature*, 633(8030):601–607, 2024.
- L. Milne-Thomson. Theoretical hydrodynamics, 1962.
- C. Pakozdi, W. Wang, A. Kamath, and H. Bihs. Reduction of the wave propagation error of a sigma grid based numerical tank using a vertical spacing based on the constant truncation error. *Ocean Engineering*, 239:109741, 2021.
- V. Ruban. Water waves over a strongly undulating bottom. *Physical Review E—Statistical, Nonlinear, and Soft Matter Physics*, 70(6):066302, 2004.
- V. P. Ruban. Water waves over a time-dependent bottom: Exact description for 2d potential flows. *Physics Letters A*, 340(1-4):194–200, 2005.
- B. R. Seiffert and G. Ducrozet. Simulation of breaking waves using the high-order spectral method with laboratory experiments: wave-breaking energy dissipation. *Ocean Dynamics*, 68:65–89, 2018.
- B. R. Seiffert, G. Ducrozet, and F. Bonnefoy. Simulation of breaking waves using the high-order spectral method with laboratory experiments: Wave-breaking onset. *Ocean Modelling*, 119:94–104, 2017.
- Z. Tian, M. Perlin, and W. Choi. Energy dissipation in two-dimensional unsteady plunging breakers and an eddy viscosity model. *Journal of Fluid Mechanics*, 655: 217–257, 2010. doi: 10.1017/S0022112010000832.
- C. Viotti, D. Dutykh, and F. Dias. The conformal-mapping method for surface gravity waves in the presence of variable bathymetry and mean current. *Procedia IUTAM*, 11:110–118, 2014.
- W. Wang, C. Pákozdi, A. Kamath, S. Fouques, and H. Bihs. A flexible fully nonlinear potential flow model for wave propagation over the complex topography of the norwegian coast. *Applied Ocean Research*, 122:103103, 2022.
- B. J. West, K. A. Brueckner, R. S. Janda, D. M. Milder, and R. L. Milton. A new numerical method for surface hydrodynamics. *Journal of Geophysical Research: Oceans*, 92(C11):11803–11824, 1987.
- G. Wu and R. E. Taylor. Time stepping solutions of the two-dimensional nonlinear wave radiation problem. *Ocean Engineering*, 22(8):785–798, 1995.
- V. E. Zakharov, A. I. Dyachenko, and O. A. Vasilyev. New method for numerical simulation of a nonstationary potential flow of incompressible fluid with a free surface. *European Journal of Mechanics-B/Fluids*, 21(3):283–291, 2002.

A Projective mapping kernels

At the core of present method is the ability to prescribe conformal maps that project surface or bathymetry states onto the domain interior. These are all represented by

the two transformation kernels

$$[\mathcal{C}_h * \mu](z) = \sum_{j=-M}^M \mathcal{F}_j(\mu) \frac{e^{ik_j(z+ih)}}{\cosh(k_j h)} = \mathcal{F}_i^{-1} \left[\mathcal{F}_j(\mu) \frac{2e^{-k_j y}}{1 + e^{2k_j h}} \right], \quad (43a)$$

$$[\mathcal{S}_h * \mu](z) = \sum_{j=-M}^M \mathcal{F}_j(\mu) \frac{e^{ik_j(z+ih)}}{\delta_j - \sinh(k_j h)} = \mathcal{F}_i^{-1} \left[\mathcal{F}_j(\mu) \frac{2e^{-k_j y}}{1 - e^{2k_j h} + 2\delta_j} \right], \quad (43b)$$

\mathcal{F}_j being the discrete Fourier transform operator $\mathcal{F}_j(\mu) = \frac{1}{n} \sum_{i=1}^n \mu(x_i, t) e^{-ik_j x_i}$ and $\mathcal{F}_i^{-1}(\{\hat{\mu}_j\}) = \sum_j \hat{\mu}_j e^{ik_j x_i}$ its inverse. Here, δ_j deals with the zero-mode and equals one if $j = 0$ and zero otherwise. The wavenumbers are defined as $k_j = 2\pi j/L$, L being the horizontal domain length. For simplicity, an odd number of points $n = 2M + 1$, uniformly spaced at a fixed depth, is here assumed. If the number of points is even, then the kernels for the highest wavenumber $k = -n\pi/L$ are $\cosh k(h - iz) \operatorname{sech} kh$ and $\sinh k(h - iz) \operatorname{csch} kh$, respectively.

Assuming $\mu(x)$ is real, the kernels (43) have the following properties:

$$[\mathcal{C}_h * \mu](x) = \mu(x) - 2i \sum_{j=1}^M \operatorname{Im} \left[\mathcal{F}_j(\mu) e^{ik_j x} \right] \tanh k_j h, \quad (44a)$$

$$[\mathcal{S}_h * \mu](x) = \mu(x) - 2i \sum_{j=1}^M \operatorname{Im} \left[\mathcal{F}_j(\mu) e^{ik_j x} \right] \coth k_j h; \quad (44b)$$

$$[\mathcal{C}_h * \mu](x - ih) = \langle \mu \rangle + 2 \sum_{j=1}^M \operatorname{Re} \left[\mathcal{F}_j(\mu) e^{ik_j x} \right] \operatorname{sech} k_j h, \quad (44c)$$

$$[\mathcal{S}_h * \mu](x - ih) = \langle \mu \rangle - 2i \sum_{j=1}^M \operatorname{Im} \left[\mathcal{F}_j(\mu) e^{ik_j x} \right] \operatorname{csch} k_j h; \quad (44d)$$

$$\lim_{h \rightarrow \infty} [\mathcal{C}_h * \mu](z) = \lim_{h \rightarrow \infty} [\mathcal{S}_h * \mu](z) = \langle \mu \rangle + 2 \sum_{j=-M}^{-1} \mathcal{F}_j(\mu) e^{ik_j z} \quad (44e)$$

$\langle \mu \rangle = \mathcal{F}_0(\mu)$ being the spatial mean. This means that the real part of both kernels equals the input function itself at the line $y = 0$, while \mathcal{C} yields pure real values and \mathcal{S} pure imaginary values at the line $y = -h$, except for a constant. The equivalent projections that map μ to the bed reference line $y = -h$ are obtained with

$$\{[\mathcal{C}_h * \mu](z^* - ih)\}^* = [\mathcal{C}_{-h} * \mu](z + ih)$$

and similar for \mathcal{S}_h .

An illustration of how the transformations can be implemented in practice is given in [Listing 3](#). This also includes demonstration of derivation and domain mirroring.

```
function convMu = convKernel(type,h,mu,z,n,MIRROR)
    nx0 = size(mu,1); x = real(z); y = imag(z); dx = x(2)-x(1);
    if MIRROR
        nx2 = 2*(nx-1);
        y = y([1:nx,nx-1:-1:2],:); % eq 8
        mu = mu([1:nx,nx-1:-1:2],:); % eq 8
    else
```

```

    nx2 = nx;
end
dk = 2*pi/(nx2*dx);
k = [0:ceil(nx2/2)-1,-floor(nx2/2):-1]*dk;
if type == 'C'
    sign = +1;
elseif type == 'S'
    sign = -1;
end
kernel = 2./(exp(k.*y)+sign*exp(k.*(2*h+y))); kernel(1) = 1; % eq A.1
if mod(nx2,2) == 0 % exception for largest even-number mode
    m = nx/2+1; y = y(m,:); km = k(m);
    kernel(m,:) = (exp(km.*(y+2*h))+sign.*exp(-km.*y))./(exp(2*km)*h)+sign
);
end
convMu = ifft(fft(mu).*(1i.*k).^n.*kernel);% evaluation including
derivative
convMu = convMu(1:nx,:); % remove mirror plane
end

```

Listing 3: Example function in MATLAB syntax returning projection mapping (43) (convolution operators) with option for derivation.